

# Gravitational clustering of relic neutrinos and implications for their detection

Andreas Ringwald and Yvonne Y. Y. Wong

Deutsches Elektronen-Synchrotron DESY, D-22607 Hamburg, Germany

**Abstract.** We study the gravitational clustering of big bang relic neutrinos onto existing cold dark matter (CDM) and baryonic structures within the flat  $\Lambda$ CDM model, using both numerical simulations and a semi-analytical linear technique, with the aim of understanding the neutrinos' clustering properties for direct detection purposes. In a comparative analysis, we find that the linear technique systematically underestimates the amount of clustering for a wide range of CDM halo and neutrino masses. This invalidates earlier claims of the technique's applicability. We then compute the approximate phase space distribution of relic neutrinos in our neighbourhood at Earth, and estimate the large scale neutrino density contrasts within the local Greisen-Zatsepin-Kuzmin zone. With these findings, we discuss the implications of gravitational neutrino clustering for scattering-based detection methods, ranging from flux detection via Cavendish-type torsion balances, to target detection using accelerator beams and cosmic rays. For emission spectroscopy via resonant annihilation of extremely energetic cosmic neutrinos on the relic neutrino background, we give new estimates for the expected enhancement in the event rates in the direction of the Virgo cluster.

E-mail: [andreas.ringwald@desy.de](mailto:andreas.ringwald@desy.de), [yvonne.wong@desy.de](mailto:yvonne.wong@desy.de)

## 1. Introduction

The standard big bang theory predicts the existence of  $10^{87}$  neutrinos per flavour in the visible universe (e.g., [1]). This is an enormous abundance unrivalled by any other known form of matter, falling second only to the cosmic microwave background (CMB) photon. Yet, unlike the CMB photon which boasts its first (serendipitous) detection in the 1960s and which has since been observed and its properties measured to a high degree of accuracy in a series of airborne/satellite and ground based experiments, the relic neutrino continues to be elusive in the laboratory. The chief reason for this is of course the feebleness of the weak interaction. The smallness of the neutrino mass also makes momentum-transfer-based detection methods highly impractical. At present, the only evidence for the relic neutrino comes from inferences from other cosmological measurements, such as big bang nucleosynthesis (BBN) and CMB together with large scale structure (LSS) data (e.g., [2]). Nevertheless, it is difficult to accept that these neutrinos will never be detected in a more direct way.

In order to design possible direct, scattering-based detection methods, a precise knowledge of the phase space distribution of relic neutrinos is indispensable. In this connection, it is important to note that an oscillation interpretation of the atmospheric and solar neutrino data (e.g., [3]) implies that at least two of the neutrino mass eigenstates are nonrelativistic today. These neutrinos are subject to gravitational clustering on existing cold dark matter (CDM) and baryonic structures, possibly causing the local neutrino number density to depart from the standard value of  $\bar{n}_\nu = \bar{n}_{\bar{\nu}} \simeq 56 \text{ cm}^{-3}$ , and the momentum distribution to deviate from the relativistic Fermi–Dirac function.

In this paper, we develop a method that will allow us to predict the phase space distribution of relic neutrinos in our local neighbourhood at Earth ( $\sim 8$  kpc from the Galactic Centre), as well as in outer space. The method systematically takes into account gravitational clustering of relic neutrinos on scales below  $\sim 5$  Mpc, and can be applied to the complete range of experimentally and observationally consistent neutrino masses. With these predictions, we determine the precise implications of relic neutrino clustering for future direct search experiments. To this end, we note that in earlier studies of relic neutrino direct detection, the neutrino number density in our local neighbourhood is either assumed to be unrealistically large, or simply left as a free parameter (e.g., [4, 5, 6]). With the emergence of the concordance flat  $\Lambda$ CDM model as the cosmological model of choice, today we are in a position to compute the relic neutrino phase space distribution within a well defined cosmological framework, and to contemplate again the prospects for their direct detection in a definitive way. Our studies here will also be useful for such investigations as relic neutrino absorption [7, 8, 9] and emission [10, 11, 12, 13, 14] spectroscopy.

The standard procedure for any gravitational clustering investigation is to solve the  $(1 + 3 + 3)$ -dimensional Vlasov, or collisionless Boltzmann, equation using  $N$ -body techniques (e.g., [15, 16, 17, 18]). However, these techniques are computationally very

expensive and necessarily come with limited resolutions. In the context of the cold+hot dark matter (CHDM) model, earlier  $N$ -body studies involving neutrinos probe their kinematic effects on structure formation from cluster and galaxy abundances on large scales (e.g., [19, 20, 21, 22]), to halo properties on small scales [23]. While the CHDM model has fallen out of favour in recent years (see, however, [24]), it is instructive to note that the halo simulation of [23] has a formal resolution of only  $\sim 100$  kpc. This is clearly inadequate for our considerations, where the scale of interest is of order 1 kpc.

In the context of the flat  $\Lambda$ CDM model, Singh and Ma (hereafter, SM) presented a novel approximate method to probe the accretion of neutrinos onto CDM halos at scales below  $\sim 50$  kpc [25]. The salient feature of this study is their use of parametric halo density profiles from high resolution, pure  $\Lambda$ CDM simulations as an external input, while the neutrino component is treated as a small perturbation whose clustering depends on the CDM halo profile, but is too small to affect it in return. Implementation of this approximation requires the neutrino mass density  $\rho_\nu$  to be much smaller than its CDM counterpart  $\rho_m$ . On cosmological scales, we know now from LSS data that the ratio  $\rho_\nu/\rho_m = \Omega_\nu/\Omega_m$  is at most  $\sim 0.2$  [2]. On cluster/galactic scales, neutrino free-streaming ensures that  $\rho_\nu/\rho_m$  always remains smaller than its cosmological counterpart [23]. Thus the approximation scheme, so far, is sound. Furthermore, in order to track the neutrino density fluctuations in the most effortless way, SM employed the linearised Vlasov equation instead of its full version. Unfortunately, linear methods are known to break down when the density fluctuations reach the order of unity. Indeed, in their two trial runs with CHDM parameters, the linear results of SM compare favourably with  $N$ -body results of [23] in the outer part of the halo, where the neutrino overdensity is relatively low. The denser inner parts ( $\lesssim 1$  Mpc), however, show marked disagreement. This discrepancy renders SM's claim that their complete prescription is able to probe neutrino clustering on sub-galactic scales doubtful.

In the present investigation, we adopt one of the more attractive features of SM's study, namely, the use of parametric halo profiles as an external input. However, we improve upon their analysis by solving the Vlasov equation in its (almost) full glory utilising a restricted,  $N$ -1-body (pronounced: EN-ONE-BODY) method based on the following observation: In the limit  $\rho_\nu \ll \rho_m$  and the CDM contribution dominates the total gravitational potential, not only will the CDM halo be gravitationally blind to the neutrinos, the neutrinos themselves will also have negligible gravitational interaction with each other. This allows us to track them one particle at a time in  $N$  independent simulations, instead of following  $N$  particles simultaneously in one single run, as in a conventional  $N$ -body study. An obvious advantage of our  $N$ -1-body technique is that it requires virtually no computing power when compared with a full scale  $N$ -body simulation with the same, large  $N$  ( $\gtrsim 10^6$ ). It is also less time-consuming since we have done away with the need for a gravity solver (the core of all  $N$ -body techniques). In addition, restricted methods such as ours do not suffer from spurious two body relaxation, and hence do not require the introduction of an artificial softening length that is mandatory in conventional  $N$ -body studies. Lastly, we note that restricted methods

have been used extensively in the studies of galaxy interactions (e.g., [26]), and, when properly motivated, should not be seen as inferior to full scale  $N$ -body techniques.

As a closing remark, let us stress again that our purpose here is not to investigate the effects of neutrino mass on cosmology, but rather to address some simple questions such as how many relic neutrinos can we realistically expect to find in this very space we occupy, what kind of energies do they have, where in the universe can we expect to find the highest concentration of relic neutrinos, etc., given what we know today about cosmology. In this regard, the analysis we present here is most exhaustive.

The paper is organised as follows. We begin in section 2 with an assessment of the current observational constraints on the relic neutrino background. In section 3, we introduce the Vlasov equation which is used to track the phase space distribution of the neutrinos. Section 4 contains a brief discussion of the halo density profiles to be employed in our calculations. In section 5, we solve the Vlasov equation for the halo models using our improved  $N$ -1-body method for a variety of halo and neutrino masses. In section 6, we compute for the same halo models and neutrino masses the neutrino overdensities using the linear method of SM and examine its validity. Section 7 deals exclusively with relic neutrinos in the Milky Way, and in particular their phase space distribution in our immediate vicinity. We discuss in section 8 the implications of our findings for scattering-based detection methods, and we conclude in section 9.

## 2. Observational constraints on the relic neutrino background

Taking as our basis (i) the flat  $\Lambda$ CDM model with  $(\Omega_{m,0}, \Omega_{\Lambda,0}) \sim (0.3, 0.7)$  and Hubble parameter  $h \sim 0.7$ , (ii) neutrino mass splittings inferred from the solar and atmospheric data,  $(\Delta m_{\text{sun}}^2, \Delta m_{\text{atm}}^2) \sim (10^{-5}, 10^{-3}) \text{ eV}^2$ , and (iii) the invisible  $Z$  decay width from LEP which constrains the number of  $SU(2)$  doublet neutrinos to three [27], a minimal theory of neutrino clustering is fixed only by the absolute masses of the neutrinos  $m_\nu$ . The current laboratory limit from tritium  $\beta$  decay experiments is  $m_\nu < 2.2 \text{ eV}$  ( $2\sigma$ ) [28, 29], and should improve to  $\sim 0.35 \text{ eV}$  with the upcoming KATRIN experiment [30]. Cosmology also provides a constraint on  $m_\nu$ . For three degenerate species, an upper bound of  $\sum m_\nu < 1.7 \text{ eV}$  ( $2\sigma$ ) [31, 32, 33] has been inferred from a combined analysis of the CMB anisotropy from WMAP [34] and galaxy clustering from SDSS (SDSS-gal) [35] (or from 2dFGRS [36]), together with an HST prior on the Hubble parameter [37]. (Reference [32] uses also SNIa [38]).<sup>‡</sup> Adding to the fit galaxy bias [39] and Ly $\alpha$  forest analyses can tighten the constraint to  $\sum m_\nu < 0.42 \text{ eV}$  [40] (see also [41, 42, 43, 44]), although the robustness of these additional inputs is still contentious. Weak lensing of galaxies [45] or of the CMB [46] will provide an alternative probe for the cosmological implications of massive neutrinos.

While constraints from cosmology are interesting in their own right, they are also highly model dependent, and degeneracies abound. For instance, if tensors and running

<sup>‡</sup> The mass splittings inferred from the solar and atmospheric neutrino oscillation experiments imply that the three mass eigenstates are quasi-degenerate when  $m_\nu \gg \sqrt{\Delta m_{\text{atm}}^2}$ .

of the scalar spectral index are allowed, the last  $\sum m_\nu$  bound relaxes to 0.66 eV [40]. Another possibility is an interplay between  $m_\nu$  and  $N_\nu$ , where  $N_\nu$  is the *effective* number of thermalised fermionic degrees of freedom present in the radiation-dominated era, such that increasing  $N_\nu$  actually weakens the bound on  $m_\nu$  [33]. For example, a  $N_\nu = 6$  model receives a CMB+LSS+priors constraint of (i)  $\sum m_\nu < 2.7$  eV, if all six particles are equally massive, (ii)  $\sum m_\nu < 2.1$  eV, if three are massive and the others exactly massless, and (iii)  $\sum m_\nu < 4.13$  eV, if only one is massive [47]. Currently,  $1.4 \leq N_\nu \leq 6.8$  is allowed by CMB+LSS+priors [33, 42, 48, 49, 50]. Future CMB experiments such as Planck will be sensitive to  $\Delta N_\nu \sim 0.2$  [51, 52]

Lastly, we note that BBN prefers  $1.84 \leq N_\nu \leq 4.54$  ( $2\sigma$ ), in the absence of a  $\nu_e$  chemical potential  $\zeta_{\nu_e}$  [53] (see also [50, 54]). Allowing for a nonzero  $\zeta_{\nu_e}$  weakens the bounds to  $1.3 \leq N_\nu \leq 7.1$  for  $-0.1 \leq \zeta_{\nu_e} \leq 0.3$  [55]. There is no lack of candidates in the literature for these extra  $N_\nu - 3$  degrees of freedom. We shall not list them here. What is certain, however, is that they cannot take the form of very large chemical potentials in the  $\nu_{\mu,\tau}$  sectors, since large neutrino mixing inferred from oscillation experiments ensures that  $\zeta_{\nu_e} \sim \zeta_{\nu_\mu} \sim \zeta_{\nu_\tau} < 0.3$ , too small to be a significant source of  $N_\nu$  [56, 57, 58].

In the present analysis, we assume the neutrinos to constitute exactly three thermalised fermionic degrees of freedom, and adopt a conservative mass bound of

$$m_\nu \lesssim 0.6 \text{ eV}, \quad (2.1)$$

corresponding to the  $N_\nu = 3$  constraint from the WMAP+SDSS galaxy cluster analysis [31]. Alternatively, (2.1) may be interpreted as a restrictive bound for models with extra, non-neutrino relativistic particles ( $N_\nu > 3$ ), or with a significant running spectral index, as discussed earlier.

### 3. Vlasov equation

A system consisting of several types of weakly interacting, self-gravitating particles [e.g., CDM plus neutrinos] may be modelled as a multi-component collisionless gas whose phase space distributions  $f_i(\mathbf{x}, \mathbf{p}, \tau)$  obey the Vlasov equation (e.g., [18, 59]),

$$\frac{Df_i}{D\tau} \equiv \frac{\partial f_i}{\partial \tau} + \dot{\mathbf{x}} \cdot \frac{\partial f_i}{\partial \mathbf{x}} + \dot{\mathbf{p}} \cdot \frac{\partial f_i}{\partial \mathbf{p}} = 0. \quad (3.1)$$

The single-particle phase density  $f_i(\mathbf{x}, \mathbf{p}, \tau)$  is defined so that  $dN_i = f_i d^3x d^3p$  is the number of  $i$  particles in an infinitesimal phase space volume element. The variables

$$\mathbf{x} = \mathbf{r}/a(t), \quad \mathbf{p} = am_i \dot{\mathbf{x}}, \quad d\tau = dt/a(t), \quad (3.2)$$

are the comoving distance, its associated conjugate momentum, and the conformal time respectively, with  $a$  as the scale factor and  $m_i$  the mass of the  $i$ th particle species. All temporal and spatial derivatives are taken with respect to comoving coordinates, i.e.,  $\dot{\ } \equiv \partial/\partial \tau$ ,  $\nabla \equiv \partial/\partial \mathbf{x}$ .<sup>§</sup> In the nonrelativistic, Newtonian limit, equation (3.1) is

<sup>§</sup> Unless otherwise indicated, we shall be using comoving spatial and temporal quantities throughout the present work. Masses and densities, however, are always physical.

equivalent to

$$\frac{\partial f_i}{\partial \tau} + \frac{\mathbf{p}}{am_i} \cdot \frac{\partial f_i}{\partial \mathbf{x}} - am_i \nabla \phi \cdot \frac{\partial f_i}{\partial \mathbf{p}} = 0, \quad (3.3)$$

with the Poisson equation

$$\nabla^2 \phi = 4\pi G a^2 \sum_i \bar{\rho}_i(\tau) \delta_i(\mathbf{x}, \tau), \quad (3.4)$$

$$\delta_i(\mathbf{x}, \tau) \equiv \frac{\rho_i(\mathbf{x}, \tau)}{\bar{\rho}_i(\tau)} - 1, \quad \rho_i(\mathbf{x}, \tau) = \frac{m_i}{a^3} \int d^3 p f_i(\mathbf{x}, \mathbf{p}, \tau), \quad (3.5)$$

relating the peculiar gravitational potential  $\phi(\mathbf{x}, \tau)$  to the density fluctuations  $\delta_i(\mathbf{x}, \tau)$  with respect to the physical mean  $\bar{\rho}_i(\tau)$ .

The Vlasov equation expresses conservation of phase space density  $f_i$  along each characteristic  $\{\mathbf{x}(\tau), \mathbf{p}(\tau)\}$  given by

$$\frac{d\mathbf{x}}{d\tau} = \frac{\mathbf{p}}{am_i}, \quad \frac{d\mathbf{p}}{d\tau} = -am_i \nabla \phi. \quad (3.6)$$

The complete set of characteristics coming through every point in phase space is thus exactly equivalent to equation (3.1). It is generally not possible to follow the whole set of characteristics, but the evolution of the system can still be traced, to some extent, if we follow a sufficiently large but still manageable sample selected from the initial phase space distribution. This forms the basis of particle-based solution methods.

#### 4. Halo density profiles and other preliminary concerns

A “first principles” approach to neutrino clustering requires the simultaneous solution of the Vlasov equation (3.1) [or, equivalently, the equations for the characteristics (3.6)] for both the CDM and the neutrino components. In our treatment, however, we assume only the CDM component  $\rho_m$  contributes to  $\phi$  in the Poisson equation (3.4), and  $\rho_m$  to be completely specified by halo density profiles from high resolution  $\Lambda$ CDM simulations. We provide in this section further justifications for this approach, as well as a brief discussion on the properties of the halo density profiles to be used in our analysis.

It is well known that after they decouple from the cosmic plasma at  $T \sim 1$  MeV, light neutrinos ( $m_\nu \ll 1$  keV) have too much thermal velocity to cluster on small scales via gravitational instability in the early stages of structure formation. Accretion onto CDM protoclusters becomes possible only after the neutrino velocity has dropped below the velocity dispersion of the protoclusters. The mean velocity of the unperturbed neutrino distribution has a time dependence of

$$\langle v \rangle \simeq 1.6 \times 10^2 (1+z) \left( \frac{\text{eV}}{m_\nu} \right) \text{ km s}^{-1}, \quad (4.1)$$

where  $z$  is the redshift. A typical galaxy cluster has a velocity dispersion of about  $1000 \text{ km s}^{-1}$  today; a typical galaxy, about  $200 \text{ km s}^{-1}$ . Thus, for sub-eV neutrinos, clustering on small scales can only have been a  $z \lesssim 2$  event.

On the other hand, based on a systematic  $N$ -body study of halo formation in a variety of hierarchical clustering cosmologies, Navarro, Frenk and White (hereafter, NFW) argued in 1996 that density profiles of CDM halos conform to a universal shape, generally independently of the halo mass, the cosmological parameters and the initial conditions [60, 61]. This so-called NFW profile has a two-parameter functional form

$$\rho_{\text{halo}}(r) = \frac{\rho_s}{(r/r_s)(1+r/r_s)^2}, \quad (4.2)$$

where  $r_s$  is a characteristic inner radius, and  $\rho_s = 4\rho(r_s)$  a corresponding inner density. These parameters  $r_s$  and  $\rho_s$  are determined by the halo's virial mass  $M_{\text{vir}}$  and a dimensionless concentration parameter  $c$  defined as

$$c \equiv \frac{r_{\text{vir}}}{r_s}, \quad (4.3)$$

where  $r_{\text{vir}}$  is the virial radius, within which lies  $M_{\text{vir}}$  of matter with an average density equal to  $\Delta_{\text{vir}}$  times the mean matter density  $\bar{\rho}_m$  at that redshift, i.e.,

$$\begin{aligned} M_{\text{vir}} &\equiv \frac{4\pi}{3} \Delta_{\text{vir}} \bar{\rho}_m a^3 r_{\text{vir}}^3 = \frac{4\pi}{3} \Delta_{\text{vir}} \bar{\rho}_{m,0} r_{\text{vir}}^3 \\ &= 4\pi \rho_s a^3 r_s^3 \left[ \ln(1+c) - \frac{c}{1+c} \right], \end{aligned} \quad (4.4)$$

where  $\bar{\rho}_{m,0}$  is the present day mean matter density. The factor  $\Delta_{\text{vir}}$  is usually taken to be the overdensity predicted by the dissipationless spherical top-hat collapse model  $\delta_{\text{TH}}$ , which takes on a value of  $\sim 178$  for an Einstein–de Sitter cosmology, while the currently favoured  $\Lambda$ CDM model has  $\delta_{\text{TH}} \simeq 337$  at  $z = 0$ .<sup>||</sup>

Within this framework, any halo density profile is completely specified by its virial mass and concentration via equations (4.2) to (4.4). Indeed, the NFW profile in its two-parameter form generally gives, for quiet isolated halos, a fit accurate to  $\sim 10\%$  in the range of radii  $r = 0.01 \rightarrow 1 r_{\text{vir}}$  [18]. Furthermore, NFW argued for a tight correlation between  $M_{\text{vir}}$  and  $c$ , such that the mass distribution within a halo is effectively fixed by the halo's virial mass alone. Later studies support, to some extent, this conclusion (e.g., [62, 63, 64]); halo concentration correlates with its mass, albeit with a significant scatter. The analysis of [64] of  $\sim 5000$  halos in the mass range  $10^{11} \rightarrow 10^{14} M_{\odot}$  reveals a trend (at  $z = 0$ ) described by

$$c(z=0) \simeq 9 \left( \frac{M_{\text{vir}}}{1.5 \times 10^{13} h^{-1} M_{\odot}} \right)^{-0.13}, \quad (4.5)$$

with a  $1\sigma$  spread about the median of  $\Delta(\log c) = 0.18$  for fixed  $M_{\text{vir}}$ . In addition, for a fixed virial mass, the median concentration parameter exhibits a redshift dependence of

$$c(z) \simeq \frac{c(z=0)}{1+z} \quad (4.6)$$

between  $z = 0$  and  $z = 4$ .

In their analysis, SM interpreted the set of equations (4.2) to (4.6) as a complete description of an individual halo's evolution in time. While we do not completely

<sup>||</sup> In the original work of NFW [60, 61],  $r_{\text{vir}}$  is taken to be the radius  $r_{200}$ , within which the average density is 200 times the *critical density* of the universe, irrespective of the cosmological model in hand.

disagree with this interpretation, it should be remembered that the relations (4.5) and (4.6) refer only to the behaviour of the statistical mean for *fixed* virial masses, and do not actually describe how individual halos accrete mass over time. A better motivation for the equations' use comes from the observation that the physical densities of the inner regions of individual isolated halos tend to remain very stable over time ( $z \sim 2 \rightarrow 0$ ) [65]. This behaviour, as it turns out, can be more or less reproduced by equations (4.2) to (4.6), if we interpret  $M_{\text{vir}}$  as the halo's virial mass today. Merging subhalos tend to affect the main halo's density profile only in its outer region. Therefore, provided that neutrino clustering becomes important only after  $z \sim 2$  and the halos have had no major mergers since then, we are justified to either use these equations here, or simply model the CDM halo as a static object in physical coordinates, as a first approximation.

Finally, we note that there exists in the literature a number of other halo profiles (e.g., [66, 67]), which, in some cases, provide better fits to simulations than does the NFW profile (4.2). However, these profiles generally differ from (4.2) by less than 10% [18] so we do not consider them in our study.

## 5. $N$ -1-body simulations

Using the NFW halo density profile (4.2) as an input, we find solutions to the Vlasov equation in the limit  $\rho_\nu \ll \rho_m$  by solving the equations for the characteristics (3.6). We discuss below the basic set-up. Technical details can be found in the Appendix.

### 5.1. Basic set-up and assumptions

We model the CDM distribution as follows. We assume that throughout space is a uniform distribution of CDM. On top of it, sits a spherical NFW halo at the origin. In order that the halo overdensity merges smoothly into the background density, we extend the NFW profile to beyond the virial radius. Furthermore, for convenience, we treat the NFW profile as a perturbation  $\bar{\rho}_m(\tau)\delta_m(\mathbf{x}, \tau)$ , rather than a physical density. This simplification should make very little difference to the final results, since the halo density is always much larger than the background density. The halo's properties and its evolution in time are contained in the set of equations (4.2) to (4.6). For the factor  $\Delta_{\text{vir}}$ , we take a time-independent value  $\Delta_{\text{vir}} = 200$ , following [68] and SM. We choose this somewhat uncommon definition so as to facilitate direct comparisons between the results of SM and those of the present study. However, since the choice of  $\Delta_{\text{vir}}$  affects the profile only through  $r_s$  [see equation (A.10) in the Appendix], we can see immediately that using instead the more common  $\Delta_{\text{vir}} = \delta_{\text{TH}}$ , where

$$\delta_{\text{TH}} \simeq \frac{18\pi^2 + 82y - 39y^2}{\Omega_m(z)}, \quad y = \Omega_m(z) - 1, \quad (5.1)$$

with  $\Omega_m(z) = \Omega_{m,0}/(\Omega_{m,0} + \Omega_{\Lambda,0}a^3)$  [69], will make little difference to the outcome.

A more important issue is the role played by other CDM structures (i.e., other halos and voids) that should realistically be in the surroundings. In our present scheme,

these have all been lumped into one uniform background so as to preserve the spherical symmetry of the problem. In reality, these structures will induce tidal forces and distort the symmetry. However, we expect tidal forces to be important only for clustering in the outer part of the halo where the gravitational potential is low and several halos may compete for the same neutrinos. Clustering in the deep potential well of the inner part, on the other hand, should not be seriously affected.

For the neutrinos, we take the initial distribution to be the homogeneous and isotropic Fermi–Dirac distribution with no chemical potential,

$$f_0(p) = \frac{1}{1 + \exp(p/T_{\nu,0})}, \quad (5.2)$$

where  $T_{\nu,0} = 1.676 \times 10^{-4}$  eV is the present day neutrino temperature. In principle, the chemical potential need not be exactly zero. In fact, a positive chemical potential  $\zeta_\nu$  should improve, to some extent, the clustering of neutrinos (as opposed to anti-neutrinos) by providing more low velocity specimens that cluster more efficiently than do their high velocity counterparts. However, this enhancement is necessarily accompanied by a suppression of clustering in the anti-neutrino sector, for which a negative  $\zeta_{\bar{\nu}} = -\zeta_\nu$  tends to deplete the low velocity states. Currently, the upper bound on  $\zeta_\nu$  is 0.3, too small to warrant a detailed investigation into a possible “clustering asymmetry”.

We simulate initial momentum values in the range  $0.01 \leq p/T_{\nu,0} \leq 13$ , which accounts for more than 99.9% of the distribution (5.2). The initial spatial positions of the neutrinos range from  $r = 0$ , to as far as it takes for the fastest particles to land within a distance of  $10 h^{-1}\text{Mpc}$  from the halo centre at  $z = 0$ . We consider a sample of three neutrino masses,  $m_\nu = 0.15, 0.3, 0.6$  eV, consistent with the bound (2.1), and a range of halo viral masses,  $M_{\text{vir}} = 10^{12}M_\odot \rightarrow 10^{15}M_\odot$ , corresponding to halos of the galaxy to the galaxy cluster variety. All simulations model a flat  $\Lambda\text{CDM}$  cosmology, with the parameters  $(\Omega_{m,0}, \Omega_{\Lambda,0}, h) = (0.3, 0.7, 0.7)$

The initial spatial and momentum distribution is divided into small chunks that move under the external potential of the CDM halo, but independently of each other. A low resolution run is first carried out for each set of  $\{m_\nu, M_{\text{vir}}\}$ . All chunks that end up at  $z = 0$  inside a sphere of radius  $10 h^{-1}\text{Mpc}$  centred on the halo are traced back to their origin, subdivided into smaller chunks, and then re-simulated. The process is repeated until the inner  $\sim 10 h^{-1}\text{kpc}$  is resolved. The initial redshift is taken to be  $z = 3$ . This should be sufficient, since clustering is not expected to be fully under way until  $z \sim 2$ . The final neutrino density distribution is constructed from the set of discrete particles via a kernel density estimation method [65, 70] outlined in the Appendix, with a maximum smoothing length of  $\sim 2 h^{-1}\text{kpc}$  in the inner  $\sim 50 h^{-1}\text{kpc}$  of the halo.

## 5.2. Results and discussions

The basic results of our  $N$ -1-body simulations are presented in Figure 1, which shows the neutrino overdensities  $n_\nu/\bar{n}_\nu$  for various sets of  $\{m_\nu, M_{\text{vir}}\}$ . A companion figure,

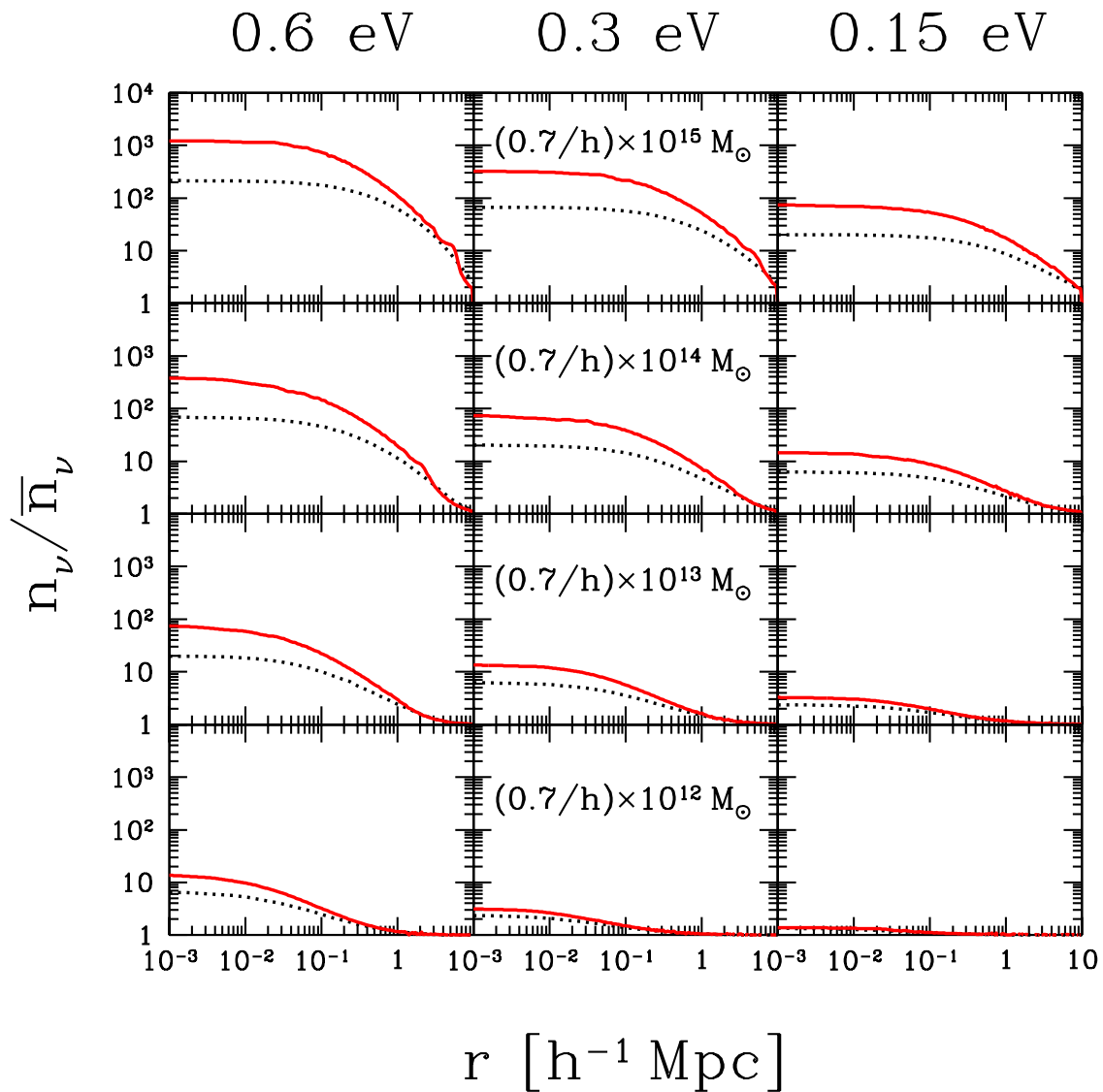


**Figure 1.** Relic neutrino number density per flavour,  $n_\nu = n_{\bar{\nu}}$ , normalised to  $\bar{n}_\nu = \bar{n}_{\bar{\nu}} \simeq 56 \text{ cm}^{-3}$ , for neutrino masses  $m_\nu = 0.6, 0.3, 0.15 \text{ eV}$  and halo virial masses indicated in the figure. Results from  $N$ -1-body simulations are denoted by red (solid) lines. Dotted lines correspond to overdensities calculated with the linear approximation.

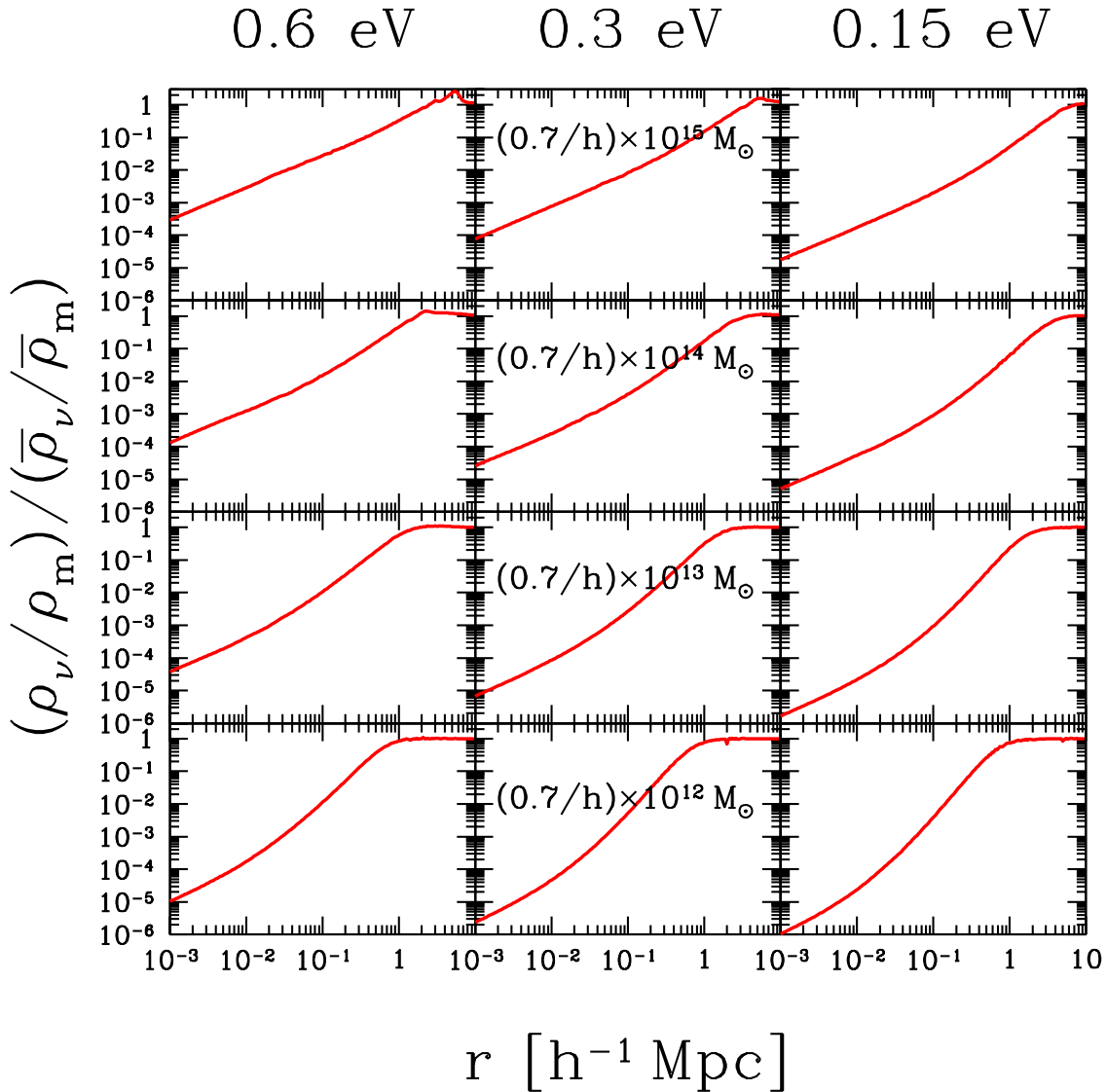


**Figure 2.** Mass density ratio  $\rho_\nu/\rho_m$  normalised to the background mean  $\bar{\rho}_\nu/\bar{\rho}_m$  obtained from  $N$ -1-body simulations for various neutrino and halo masses indicated in the figure.

Figure 2, shows the same results expressed in terms of the mass density ratio  $\rho_\nu/\rho_m$  normalised to the background mean  $\bar{\rho}_\nu/\bar{\rho}_m$ .

The essential features of the curves in Figures 1 and 2 can be understood in terms of neutrino free-streaming, which causes the  $n_\nu/\bar{n}_\nu$  curves to flatten out at small radii, and the mass density ratio  $\rho_\nu/\rho_m$  to drop substantially below the background mean. (The latter feature also provides a justification for our  $N$ -1-body method.) Both  $n_\nu/\bar{n}_\nu$  and  $\rho_\nu/\rho_m$  approach their respective cosmic mean of 1 and  $\bar{\rho}_\nu/\bar{\rho}_m$  at large radii. Similar behaviours have also been observed in the CHDM simulations of reference [23].

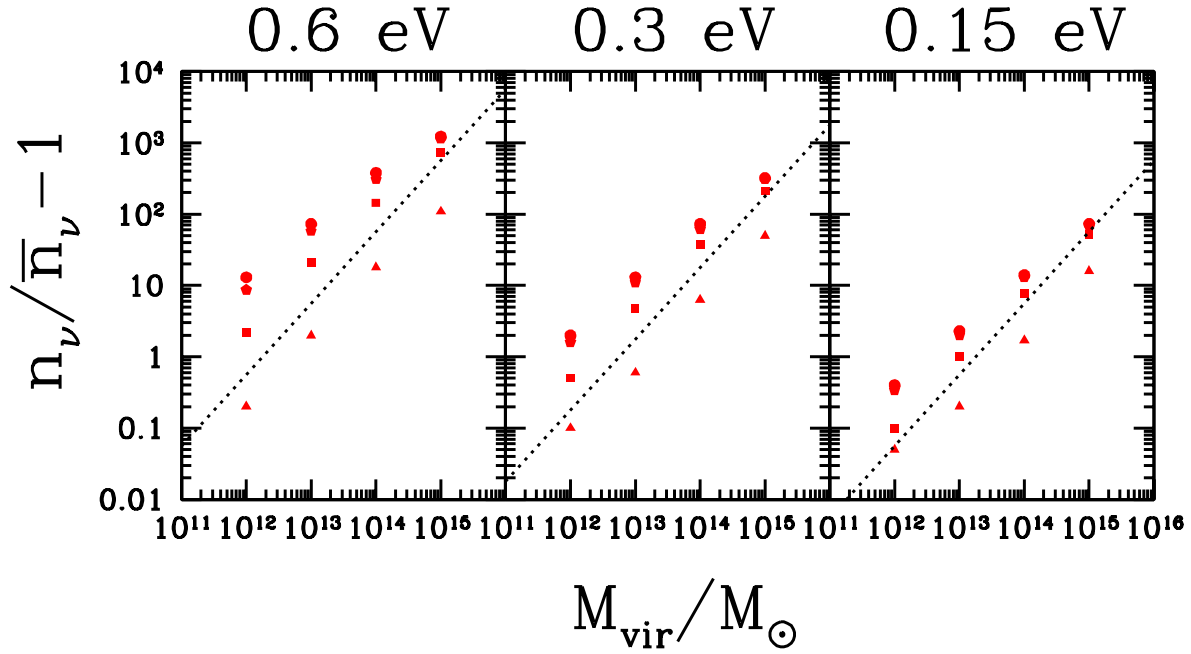


**Figure 3.** Dependence of the neutrino overdensity on the halo virial mass for neutrino masses  $m_\nu = 0.6, 0.3, 0.15$  eV. The circles represent overdensities at  $1 h^{-1}\text{kpc}$ , pentagons at  $10 h^{-1}\text{kpc}$ , squares at  $100 h^{-1}\text{kpc}$  and triangles at  $1000 h^{-1}\text{kpc}$ . The straight lines ( $\propto M_{\text{vir}}$ ) are provided to guide the eye and are *not* meant to be best fits.

Naturally, clustering improves with increasing neutrino and/or halo masses. In Figure 3, we plot the neutrino overdensities at  $1, 10, 100, 1000 h^{-1}\text{kpc}$  for various neutrino masses as a function of the halo virial mass  $M_{\text{vir}}$ . A similar plot is constructed in Figure 4, with the neutrino mass  $m_\nu$  as the independent variable. In the former, the quantity  $n_\nu/\bar{n}_\nu - 1$  is seen to be roughly proportional to  $M_{\text{vir}}$  for a fixed radius and a fixed neutrino mass. The  $n_\nu/\bar{n}_\nu - 1$  versus  $m_\nu$  trend in Figure 4 is more difficult to quantify. A roughly  $m_\nu^2$  dependence can be discerned for some fixed halo masses at some fixed radii. Other combinations, however, display noticeably different behaviours. Whatever these dependences are, it is interesting to note that they are never shallower than  $\propto m_\nu$ , or steeper than  $\propto m_\nu^3$ . As we shall see later, an  $m_\nu^2$  and an  $m_\nu^3$  dependence for the overdensities can both be motivated from theory. The former can be derived from the linearised Vlasov equation (cf. section 6), while the latter follows naturally from phase space considerations (or the so-called Tremaine–Gunn bound, cf. section 7).

Lastly, in order to test the robustness of our results, we (i) push the initial redshift of the simulations back to  $z = 5$ , (ii) vary the cosmological parameters within their allowed ranges, and (iii) alter the time dependences of some of the halo parameters. In all cases, we find, as expected, the heavier masses  $\{m_\nu, M_{\text{vir}}\}$  to suffer more from these variations. For our heaviest set,  $\{m_\nu = 0.6 \text{ eV}, M_{\text{vir}} = 0.7 \times 10^{15} h^{-1} M_\odot\}$ , the neutrino overdensity changes by about 10 to 20% at small radii, and some 50 to 100% at

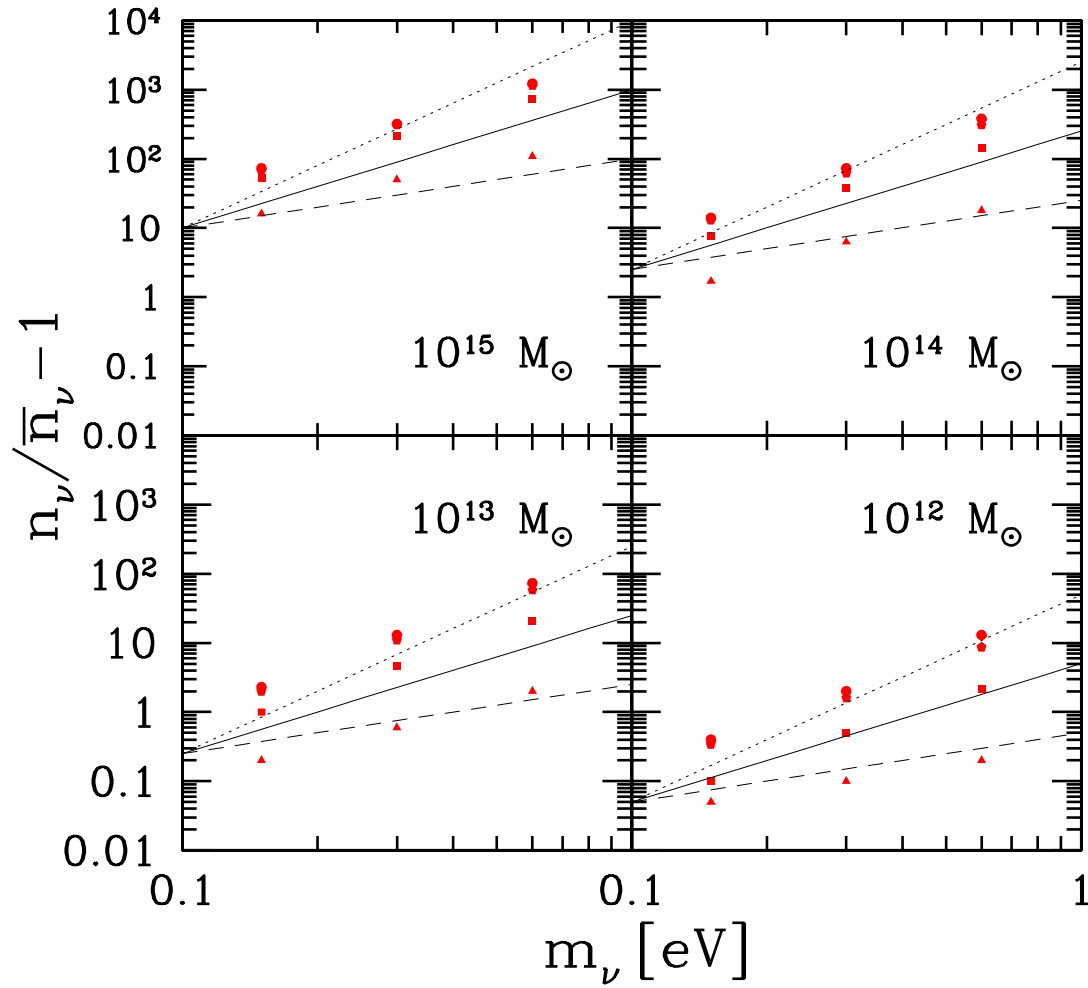


**Figure 4.** Dependence of the neutrino overdensity on the neutrino mass for various halo masses indicated on the plots. The circles represent overdensities at  $1 h^{-1}\text{kpc}$ , pentagons at  $10 h^{-1}\text{kpc}$ , squares at  $100 h^{-1}\text{kpc}$  and triangles at  $1000 h^{-1}\text{kpc}$ . The solid lines correspond to an  $m_\nu^2$  dependence, dashed lines an  $m_\nu$  dependence, and dotted lines an  $m_\nu^3$  dependence. These lines are provided to guide the eye and are *not* meant to be best fits.

$r \gtrsim 5 h^{-1}\text{Mpc}$ . The gap narrows with smaller neutrino and halo masses. For galaxy size halos ( $M_{\text{vir}} \sim 10^{12}M_{\odot}$ ), the density variations with respect to (i), (ii) and (iii) are no more than  $\sim 10\%$  everywhere. Thus our simulation results are generally quite robust.

## 6. Linear approximation

The linear approximation is often used in the literature to find approximate solutions to the Vlasov equation. In the nonrelativistic limit, the pioneering work of Gilbert [71] has, over the years, been applied to the study of the pure hot dark matter (HDM) model [72], as well as in the analysis of HDM accretion onto nonadiabatic seeds such as cosmic strings [73, 74, 75] and onto CDM halos [25]. The procedure consists of first switching to a new time variable  $s \equiv \int a^{-1}d\tau = \int a^{-2}dt$ , and then Fourier transforming the  $\mathbf{x}$ -dependent functions,

$$\hat{f}(\mathbf{k}, \mathbf{p}, s) \equiv \mathcal{F}[f(\mathbf{x}, \mathbf{p}, s)], \quad \hat{\phi}(\mathbf{k}, s) \equiv \mathcal{F}[\phi(\mathbf{x}, s)], \quad (6.1)$$

to obtain a new differential equation in Fourier space,

$$\frac{\partial \hat{f}}{\partial s} + \frac{i\mathbf{k} \cdot \mathbf{p}}{m_{\nu}} \hat{f} - im_{\nu}a^2(\mathbf{k} \hat{\phi} \star \nabla_{\mathbf{p}} \hat{f}) = 0, \quad (6.2)$$

where  $\mathbf{k} \hat{\phi} \star \nabla_{\mathbf{p}} \hat{f} \equiv \int d^3\mathbf{k}' \mathbf{k}' \hat{\phi}(\mathbf{k}') \cdot \nabla_{\mathbf{p}} \hat{f}(\mathbf{k} - \mathbf{k}')$  is the convolution product. The equation is said to be linearised when one makes the replacement

$$\nabla_{\mathbf{p}} \hat{f}(\mathbf{k}) \rightarrow \nabla_{\mathbf{p}} f_0(p) \delta(\mathbf{k}), \quad (6.3)$$

where  $\delta(\mathbf{k})$  is the Dirac delta function, so that the convolution product becomes a simple scalar product  $\mathbf{k} \hat{\phi} \cdot \nabla_{\mathbf{p}} f_0$ . Replacement (6.3) is valid as long as the condition  $|\nabla_{\mathbf{p}}(f - f_0)| \ll |\nabla_{\mathbf{p}} f_0|$  holds. In practice, however, the quantity  $\nabla_{\mathbf{p}} f$  is somewhat cumbersome to compute, so the ‘‘rule of thumb’’ regarding the linear approximation is to abandon it as soon as the spatial density fluctuation  $\delta_{\nu}(\mathbf{x}, s)$ , defined in (3.5), exceeds order unity, as emphasised in [59, 74]. Nonetheless, the linear theory has been time and again used beyond this putative limit. We shall also apply it to our case, to gain physical insight as well as to see how it compares with  $N$ -1-body simulations.

Equation (6.2) together with the replacement (6.3) has a very simple solution,

$$\begin{aligned} \hat{f}(\mathbf{k}, \mathbf{p}, s) &= \hat{f}(\mathbf{k}, \mathbf{p}, s_i) e^{-i\mathbf{k} \cdot \mathbf{u}(s-s_i)} \\ &\quad + im_{\nu} \mathbf{k} \cdot \nabla_{\mathbf{p}} f_0 \int_{s_i}^s ds' a^2(s') \hat{\phi}(\mathbf{k}, s') e^{-i\mathbf{k} \cdot \mathbf{u}(s-s')}, \end{aligned} \quad (6.4)$$

where  $\mathbf{u} = \mathbf{p}/m_{\nu}$ ,  $s_i$  is some initial time, and we take the initial phase space distribution to be isotropic and homogeneous in space, i.e.,  $\hat{f}(\mathbf{k}, \mathbf{p}, s_i) = \delta(\mathbf{k}) f_0(p)$ . The neutrino number density per Fourier mode relative to the mean density is obtained by integrating (6.4) over momenta  $\mathbf{p}$ ,

$$\begin{aligned} \frac{\hat{n}_{\nu}(\mathbf{k}, s)}{\bar{n}_{\nu}(s)} &= \frac{a^{-3} \int d^3p \hat{f}(\mathbf{k}, \mathbf{p}, s)}{a^{-3} \int d^3p f_0(p)} \equiv \frac{1}{\bar{n}_{\nu,0}} \int d^3p \hat{f}(\mathbf{k}, \mathbf{p}, s) \\ &= \delta(\mathbf{k}) - k^2 \int_{s_i}^s ds' a^2(s') \hat{\phi}(\mathbf{k}, s') (s - s') F \left[ \frac{k(s - s')}{m_{\nu}} \right], \end{aligned} \quad (6.5)$$

**Table 1.** Some distribution functions  $f_0(p)$  and their corresponding  $F(q)$  [equation (6.6)] that have appeared in the literature. The series solution for  $F(q)$  for the relativistic Fermi–Dirac (FD) function was first derived in [74]. A Maxwell–Boltzmann (MB) type distribution was adopted in [73]. The last family of distributions, characterised by  $F(q)$ ’s exponential form, appears in [59] and [76].

Distribution	$f_0(p)$	$F(q)$
Relativistic FD	$[1 + \exp(p/T_{\nu,0})]^{-1}$	$\frac{4}{3\zeta(3)} \sum_{n=1}^{\infty} (-1)^{n+1} n(n^2 + q^2 T_{\nu,0}^2)^{-2}$
MB	$\exp(-p/T_{\nu,0})$	$(1 + q^2 T_{\nu,0}^2)^{-2}$
$\gamma$ distribution	$\frac{\bar{n}_{\nu,0}}{\pi^2 (\gamma T_{\nu,0})^3} (1 + p^2/\gamma^2 T_{\nu,0}^2)^{-2}$	$\exp(-\gamma q T_{\nu,0})$

with

$$F(q) \equiv \frac{1}{\bar{n}_{\nu,0}} \int d^3p e^{-i\mathbf{p}\cdot\mathbf{q}} f_0(p). \quad (6.6)$$

The correct form for  $f_0(p)$  should be the relativistic Fermi–Dirac function (5.2), which gives for  $F(q)$  a series representation [74]

$$F(q) = \frac{4}{3\zeta(3)} \sum_{n=1}^{\infty} (-1)^{n+1} \frac{n}{(n^2 + q^2 T_{\nu,0}^2)^2}, \quad (6.7)$$

where  $\zeta(3) \simeq 1.202$  is the Riemann zeta function. However, in order to simplify calculations and/or to gain physical insight, other forms of  $f_0(p)$  have also appeared in the literature. Some are listed in Table 1, along with their corresponding  $F(q)$ .

The solution to the Poisson equation (3.4) in Fourier space is

$$\hat{\phi}(\mathbf{k}, s) = -\frac{4\pi G a^2 \bar{\rho}_m(s) \hat{\delta}_m(\mathbf{k}, s)}{k^2} = -\frac{4\pi G \bar{\rho}_{m,0} \hat{\delta}_m(\mathbf{k}, s)}{a k^2}. \quad (6.8)$$

Substituting this into (6.5) and using the definition  $\hat{\delta}_\nu(\mathbf{k}, s) \equiv \hat{n}_\nu(\mathbf{k}, s)/\bar{n}_\nu(s) - \delta(\mathbf{k})$ , we obtain for the neutrino density fluctuations

$$\hat{\delta}_\nu(\mathbf{k}, s) \simeq 4\pi G \bar{\rho}_{m,0} \int_{s_i}^s ds' a(s') \hat{\delta}_m(\mathbf{k}, s') (s - s') F \left[ \frac{k(s - s')}{m_\nu} \right]. \quad (6.9)$$

This is the “master equation” for the linear approach. We solve equation (6.9) numerically for a variety of neutrino and halo masses. The results are presented in Figure 1, alongside their  $N$ -1-body counterparts.

### 6.1. Further approximations and analytical insights

Before comparing the two approaches, let us first study the linear approximation for its own sake. Consider the master equation (6.9). In the limit  $F(q)$  grows much faster than  $a(s)$  and  $\hat{\delta}_m(\mathbf{k}, s)$ , i.e.,

$$\frac{k T_{\nu,0}}{m_\nu} \gg \frac{1}{a} \frac{da}{ds} + \frac{1}{\hat{\delta}_m} \frac{d\hat{\delta}_m}{ds}, \quad (6.10)$$

equation (6.9) may be solved by asymptotic expansion. The resulting approximate solution looks somewhat messy at first sight,

$$\hat{\delta}_\nu(\mathbf{k}, s) \simeq 4\pi G \bar{\rho}_{m,0} \left( \frac{m_\nu}{k T_{\nu,0}} \right)^2 \frac{2}{3\zeta(3)} [\ln(2)a(s)\hat{\delta}_m(\mathbf{k}, s) - a(s_i)\hat{\delta}_m(\mathbf{k}, s_i) \sum_{n=1}^{\infty} (-1)^{n+1} \frac{n}{n^2 + \frac{k^2 T_{\nu,0}^2}{m_\nu^2} (s - s_i)^2}], \quad (6.11)$$

but may be rendered into a physically transparent form if we first cross out the second term, which is well justified since the initial  $a$  and  $\hat{\delta}_m$  should always be much smaller than the final ones, and then rewrite the expression as

$$\hat{\delta}_\nu(\mathbf{k}, s) \simeq \frac{k_{\text{fs}}^2(s)}{k^2} \hat{\delta}_m(\mathbf{k}, s). \quad (6.12)$$

Here,  $k_{\text{fs}}$  is but the free-streaming wave vector, defined as

$$\begin{aligned} k_{\text{fs}}(s) &\equiv \sqrt{\frac{4\pi G a(s) \bar{\rho}_{m,0}}{c_{\nu,0}^2}} = \sqrt{\frac{4\pi G a^2(s) \bar{\rho}_m(s)}{c_\nu^2(s)}} \\ &\simeq 1.5 \sqrt{a(s) \Omega_{m,0}} \left( \frac{m_\nu}{\text{eV}} \right) h \text{ Mpc}^{-1}, \end{aligned} \quad (6.13)$$

and we identify

$$\begin{aligned} c_\nu(s) &\equiv \frac{T_{\nu,0}}{m_\nu a(s)} \sqrt{\frac{3\zeta(3)}{2 \ln(2)}} \equiv \frac{c_{\nu,0}}{a(s)} \\ &\simeq \frac{81}{a(s)} \left( \frac{\text{eV}}{m_\nu} \right) \text{ km s}^{-1} \end{aligned} \quad (6.14)$$

as the neutrino's characteristic thermal speed.

The functional form of equation (6.12) already tells us something very interesting; large Fourier modes in the neutrino density fluctuations are suppressed by a factor proportional to  $k^{-2}$  relative to their CDM counterparts. This is clearly a manifestation of free-streaming, which is responsible for inhibiting the growth of structures on scales below  $\lambda_{\text{fs}} \equiv 2\pi/k_{\text{fs}}$ . Furthermore,  $\hat{\delta}_\nu$  has an  $m_\nu^2$  dependence through  $k_{\text{fs}}$ , meaning that, at small scales, a neutrino twice as heavy as another is able to cluster four times more efficiently. This  $m_\nu^2$  dependence is reflected, approximately, by both our linear and  $N$ -1-body results in Figure 1, and is particularly pronounced at small radii.

That equation (6.12) is a solution of (6.9) is contingent upon the satisfaction of the condition (6.10), which requires, for a fixed neutrino mass,  $k$  to be larger than some nominal  $k_{\text{min}}$  determined by the rates of change of the scale factor  $a$  and of the CDM perturbations  $\hat{\delta}_m(\mathbf{k}, s)$ . The rate of change of  $a$  is a simple and well defined function of the cosmological model. The growth rate of  $\hat{\delta}_m(\mathbf{k}, s)$ , on the other hand, is usually more complicated. However, because our halos are practically static in physical coordinates, this rate (in comoving Fourier space) can only be at most of the order of the universal expansion rate (which comes in through the conversion factor  $a$  when

we switch the halo profile from physical to comoving coordinates). Thus the condition (6.10) is roughly equivalent to

$$k \gg k_{\min}(s) \sim \frac{m_\nu}{T_{\nu,0}} a^2 H(s) \simeq 2\sqrt{a\Omega_{m,0} + a^4\Omega_{\Lambda,0}} \left(\frac{m_\nu}{\text{eV}}\right) h \text{ Mpc}^{-1}, \quad (6.15)$$

where  $H(s)$  is the Hubble expansion parameter at time  $s$ . Since  $k_{\min} \sim k_{\text{fs}}$  at most times, we see that equation (6.12) is indeed applicable to all  $k$  modes larger than the free-streaming wave vector  $k_{\text{fs}}$ .

Unfortunately, the opposite  $k \ll k_{\text{fs}}$  limit has no simple approximate solution because of the complicated dependence of the scale factor  $a$  on the new time variable  $s$ . However, we find the following formula to give a decent fit to the solution of (6.9) for a wide range of  $k$ ,

$$\hat{\delta}_\nu(\mathbf{k}, s) \simeq \frac{k_{\text{fs}}^2}{(k_{\text{fs}}/\Gamma + k)^2} \hat{\delta}_m(\mathbf{k}, s) \equiv \hat{K}(k_{\text{fs}}^{-1}\mathbf{k}, s) \hat{\delta}_m(\mathbf{k}, s), \quad (6.16)$$

with

$$\Gamma^2 \equiv \frac{4\pi G \bar{\rho}_{m,0}}{\hat{\delta}_m(\mathbf{k}, s)} \int_{s_i}^s ds' a(s') \hat{\delta}_m(\mathbf{k}, s') (s - s') \Big|_{\mathbf{k} \rightarrow 0}. \quad (6.17)$$

Typically,  $\Gamma \sim 1$ , such that for  $k \ll k_{\text{fs}}$ , the growth of  $\hat{\delta}_\nu$  approximately matches that of  $\hat{\delta}_m$ . Therefore, equation (6.16) is roughly equivalent to

$$\rho_\nu(\mathbf{x}) \sim k_{\text{fs}}^3 K(k_{\text{fs}}\mathbf{x}) \star \rho_m(\mathbf{x}), \quad (6.18)$$

in real space, with  $K(\mathbf{x}) \equiv \mathcal{F}^{-1}[\hat{K}(\mathbf{k})]$  acting like a normalised filter function with window width  $k_{\text{fs}}^{-1}$ , that gently smears out the neutrino density contrasts on scales below  $\sim k_{\text{fs}}^{-1}$  relative to their CDM counterparts. We shall be using equation (6.18) again in section 8.2.

## 6.2. Comparison with $N$ -1-body results: when and how the linear theory fails

Comparing the linear results from this section with  $N$ -1-body simulations from section 5, it is immediately clear in Figure 1 that the former systematically underestimates the neutrino overdensities over the whole range of neutrino and halo masses considered in this study. The discrepancy is most prominent in the dense, inner regions ( $r \lesssim 1 h^{-1}\text{Mpc}$ ), and worsens as we increase (i) the neutrino mass  $m_\nu$ , and (ii) the halo mass  $M_{\text{vir}}$ . The worst case corresponds to when both  $m_\nu$  and  $M_{\text{vir}}$  are large; the case of  $\{m_\nu = 0.6 \text{ eV}, M_{\text{vir}} = 0.7 \times 10^{15} h^{-1} M_\odot\}$ , for example, sees the  $N$ -1-body and the linear overdensities differ by a factor of about six. For smaller neutrino and halo masses, concordance between the two approaches improves as we move to larger radii. Indeed, for  $\{m_\nu = 0.15 \text{ eV}, M_{\text{vir}} = 0.7 \times 10^{12} h^{-1} M_\odot\}$ , complete agreement is seen throughout the region of interest. Upon closer inspection, one finds that the linear theory ceases to be a faithful approximation once the neutrino overdensity reaches a value of about three or four. This is of course fully consistent with the standard lore that perturbative methods fail once the perturbations exceed unity and nonlinear effects set in.

Can the linear approximation be salvaged? Yes, provided we impose a great deal of smoothing. In the case of  $\{m_\nu = 0.6 \text{ eV}, M_{\text{vir}} = 0.7 \times 10^{15} h^{-1} M_\odot\}$ , for example, the overdensities computed from the two different approaches can be reconciled with each other if we smooth them both over a scale of roughly  $5 h^{-1} \text{Mpc}$ . Such a large smoothing length will render the linear method completely useless for the study of neutrino clustering on sub-galactic scales (unless of course the neutrino mass is so small that the overdensity does not exceed unity by much anyway). But the method can still be useful for obtaining quick estimates of  $n_\nu/\bar{n}_\nu$  on larger scales for absorption and emission spectroscopy calculations (cf. section 8.2).

Finally, we note that the neutrino overdensities in Figure 2 of SM are at odds with our linear results in Figure 1. This discrepancy cannot be ameliorated by simply supposing that SM have normalised their neutrino densities for *three* flavours to the *one* flavour average  $\bar{n}_\nu = \bar{n}_{\bar{\nu}} \simeq 56 \text{ cm}^{-3}$ , since this normalisation will render some of their results—specifically, where  $n_\nu/\bar{n}_\nu < 3$ —unphysical. Only a normalisation to *three* flavours can give these results a physical meaning, but at the expense of incompatibility with our Figure 1, as well as with SM’s own Figure 3. We therefore conclude that SM’s results as presented in their Figure 2 are erroneous.

## 7. Relic neutrinos in the Milky Way

In this section, we consider relic neutrino clustering in the Milky Way. We compute explicitly the number of neutrinos and their distribution in momentum space in our local neighbourhood at Earth ( $r_\oplus \sim 8 \text{ kpc}$  from the Galactic Centre). This information is essential for any direct search experiment.

### 7.1. Background, basic set-up and assumptions

We perform this calculation using the  $N$ -1-body method of section 5, but with a few modifications to the external potential. Firstly, we note that the central region of the Milky Way ( $\lesssim 10 \text{ kpc}$ ) is dominated by baryonic matter in the form of a disk, a bulge, and possibly a rapidly rotating bar [77]. Each of these components has its own distinct density profile. Furthermore, in the standard theory of hierarchical galaxy formation, baryons and dark matter are initially well mixed, and collapse together to form halos via gravitational instability. Galactic structures arise when the baryons cool and fall out of the original halo towards the centre [78]. As the baryons condense, their gravitational forces tend to pull the dark matter inward, thereby distorting the inner  $\sim 10 \text{ kpc}$  of the original halo profile (e.g., [79, 80, 81, 82]). This kind of modification to the mass distribution is important for us at  $r_\oplus$ . Fortunately for our calculation, gravitating neutrinos do not distinguish between halo and baryons. Therefore, it suffices to use simply the total mass distribution inferred from observational data (e.g., rotation curves, satellite kinematics, etc.), without any detailed modelling of the individual components.

What is still missing, however, is the redshift dependence of the mass distribution.

Unfortunately, we have not been able to find in the literature any simple parametric form for this dependence. However, mass modelling of the Milky Way [83, 84] suggests that certain observationally acceptable bulge+disk+halo models are indeed consistent with the aforementioned theory of baryonic compression, and can be traced back to halos *originally* of the NFW form by supposing that the system has undergone a phase of adiabatic contraction [79]. Thus, for our investigation, it is probably fair to think of the NFW profile as the initial mass distribution, and the evolution as a smooth transition from this initial distribution to the present day one.

Instead of modelling this transition, however, our strategy here is to conduct two series of simulations, one for the present day mass distribution of the Milky Way (MWnow) which we assume to be static, and one for the NFW halo (NFWhalo) that would have been there, had baryon compression not taken place. The real neutrino overdensity should then lie somewhere between these two extremes.

For the NFWhalo run, we use the parameters  $M_{\text{vir}} = 1 \times 10^{12} M_{\odot}$  and  $c = 12$ . These numbers are taken from the paper of Klypin, Zhao and Somerville (hereafter, KZS) [84], from their “favoured” mass model of the Milky Way. Note that we are not using the  $c$ - $M_{\text{vir}}$  relation (4.5), which, as we discussed before, is only a statistical trend. However, the concentration parameter  $c$  should still carry a redshift dependence *à la* equation (4.6), in order to reproduce the correct time dependence of the density profile.

For MWnow, we adopt the total mass distribution (halo+disk+bulge) presented in Figure 3 of KZS, and fit it approximately to a power law from  $r = 0$  to 20 kpc,

$$M_{\text{fit}}(r, z = 0) = 2 \times 10^{11} \left( \frac{r}{20 \text{ kpc}} \right)^{1.19367} M_{\odot}, \quad (7.1)$$

where  $M(r)$  means the total mass contained within a radius  $r$ . We assume this fit to hold for the region inside a *physical* radius of 20 kpc at all times, i.e.,  $M_{\text{fit}}(r, z) = M_{\text{fit}}(ar, z = 0)$ . The region outside of this 20 kpc sphere is not affected by baryonic compression according to the KZS mass model (cf. their Figure 7) so we adopt the original NFW density profile outwardly from 20 kpc. Thus, schematically, we have

$$\begin{aligned} M(r, r < r_0) &= M_{\text{fit}}(r), \\ M(r, r \geq r_0) &= M_{\text{NFW}}(r) - M_{\text{NFW}}(r_0) + M_{\text{fit}}(r_0), \end{aligned} \quad (7.2)$$

where  $r_0 = 20 a^{-1}$  kpc,  $M_{\text{NFW}}(r)$  is the mass contained in an NFW halo at radius  $r$  [or  $M_{\text{halo}}(r)$  in equation (A.7)], and  $M_{\text{fit}}(r_0) \simeq 2 \times M_{\text{NFW}}(r_0)$  for the parameters used in this analysis.

## 7.2. Results and discussions

Our Milky Way simulation results for four neutrino mass  $m_{\nu} = 0.15, 0.3, 0.45, 0.6$  eV are displayed in Figure 5. The shaded region in each plot corresponds to a possible range of overdensities at  $z = 0$ . At first glance, it may seem unphysical that the apparently static MWnow potential (in *physical coordinates*) should capture so many neutrinos. To resolve this “paradox”, one must remember that neutrino clustering is studied in the

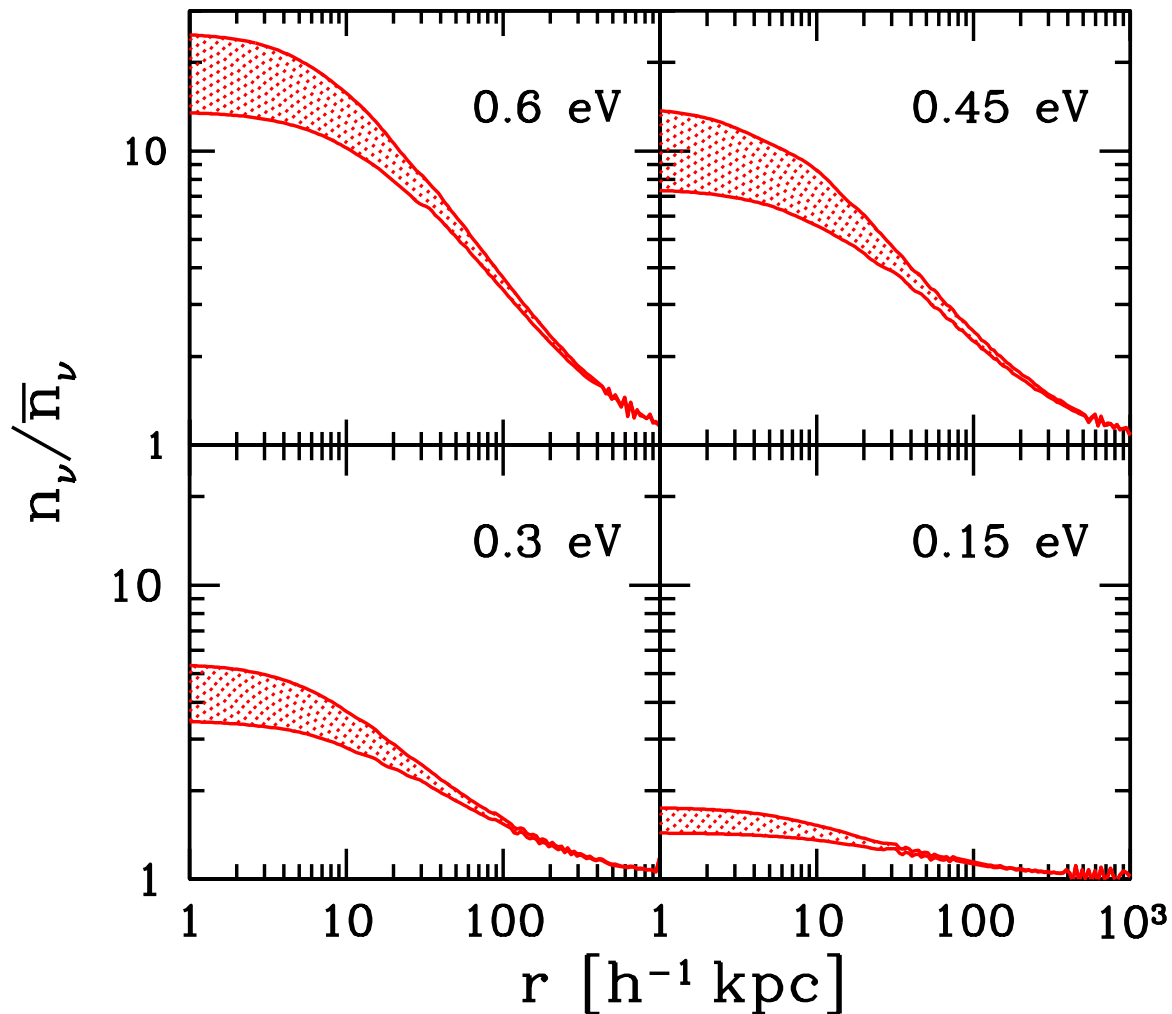


**Figure 5.** Relic neutrino number density per flavour,  $n_\nu = n_{\bar{\nu}}$ , in the Milky Way for various neutrino masses. All curves are normalised to  $\bar{n}_\nu = \bar{n}_{\bar{\nu}} \simeq 56 \text{ cm}^{-3}$ . The top curve in each plot corresponds to the MWnow run, and the bottom to the NFWhalo run. The enclosed region represents a possible range of overdensities at  $z = 0$ .

context of an expanding universe; the (unbound) neutrino thermal velocity decreases with time [equation (4.1)], thus causing them to be more readily captured. Equivalently, in *comoving coordinates*, it is easy to see that while the neutrino conjugate momentum (3.2) does not redshift, the MWnow potential well shrinks in size and deepens with time.

In each scenario we studied, the final momentum distribution at  $r_\oplus$  is almost isotropic, with a zero mean radial velocity  $\langle v_r \rangle$ , and second velocity moments that satisfy approximately the relation  $2\langle v_r^2 \rangle = \langle v_T^2 \rangle$  (cf. Table 2). For this reason, we plot

**Table 2.** Velocity moments at  $r_\oplus$  for various neutrino masses in the MWnow and NFWhalo runs (see text for definitions). The first column shows the overdensities  $n_\nu/\bar{n}_\nu$ . The second, third and fourth columns show the mean radial, transverse and absolute velocities in terms of the dimensionless quantities  $\langle y_r \rangle$ ,  $\langle y_T \rangle$  and  $\langle y \rangle$ , where  $y = m_\nu v/T_{\nu,0}$ . In the last three columns are the second moments. The corresponding values for a relativistic Fermi–Dirac distribution are displayed in the first row.

	$n_\nu/\bar{n}_\nu$	$\langle y_r \rangle$	$\langle y_T \rangle$	$\langle y \rangle$	$\langle y_r^2 \rangle$	$\langle y_T^2 \rangle$	$\langle y^2 \rangle$
Relativistic Fermi–Dirac	1	0	2.48	3.15	4.31	8.63	12.94
NFWhalo, $m_\nu = 0.6$ eV	12	0.0	3.4	4.3	6.9	13	20
NFWhalo, $m_\nu = 0.45$ eV	6.4	0.0	2.8	3.5	4.6	9.5	14
NFWhalo, $m_\nu = 0.3$ eV	3.1	0.0	2.3	3.0	3.6	7.3	11
NFWhalo, $m_\nu = 0.15$ eV	1.4	0.0	2.3	2.0	3.8	7.6	11
MWnow, $m_\nu = 0.6$ eV	20	0.0	4.0	5.1	9.3	18	28
MWnow, $m_\nu = 0.45$ eV	10	0.0	3.1	4.0	6.1	12	18
MWnow, $m_\nu = 0.3$ eV	4.4	0.0	2.5	3.2	3.9	8.0	12
MWnow, $m_\nu = 0.15$ eV	1.6	0.0	2.3	2.9	3.7	7.3	11

the smoothed, or coarse-grained, phase space densities  $\bar{f}(r_\oplus, p)$  only as functions of the absolute velocity (cf. Figure 6).

As expected, the coarse-grained distribution  $\bar{f}(r_\oplus, p)$  for the case with the highest overdensity (MWnow,  $m_\nu = 0.6$  eV) resembles the original Fermi–Dirac spectrum the least, while  $\bar{f}$  for the case with the lowest overdensity (NFWhalo,  $m_\nu = 0.15$  eV) is almost Fermi–Dirac-like. All spectra share the feature that they are flat at low momenta, with a common value of  $\sim 1/2$ . The turning point for each distribution coincides approximately with the “escape momentum”  $p_{\text{esc}}$  (i.e.,  $m_\nu$  times the escape velocity  $v_{\text{esc}} = \sqrt{2|\phi(r_\oplus)|}$ ) for the system concerned, beyond which the phase space density falls off rapidly, until it matches again the Fermi–Dirac function at the very high momentum end of the spectrum. Deviation from the original Fermi–Dirac spectrum is therefore most severe around  $p_{\text{esc}}$ .

The maximum value of  $\bar{f}$  is a little less than  $1/2$ . This is consistent with the requirement that the final coarse-grained density must not exceed the maximal value of the initial fine-grained distribution,  $\bar{f} \leq \max(f_0)$  [85]. For neutrinos,  $f_0$  has a value of  $1/2$  at  $p = 0$ . Thus, our  $\bar{f}$  not only satisfies but completely saturates the bound at low momenta up to  $p_{\text{esc}}$ , forming a kind of semi-degenerate state that can only be made denser by filling in states above  $p_{\text{esc}}$ .¶ However, since neutrinos with momenta above  $p_{\text{esc}}$  do not become gravitationally bound to the galaxy/halo, these high momentum states are much less likely to be fully occupied. This explains  $\bar{f}$ ’s rapid drop beyond  $p_{\text{esc}}$ . Also, the hottest neutrinos are not significantly affected by the galaxy/halo’s gravitational forces. Therefore the very high end of the momentum distribution remains more or less Fermi–Dirac-like. Finally, we note that because the filling of phase space happens from

¶ This degeneracy should not be confused with that arising from the Pauli exclusion principle.

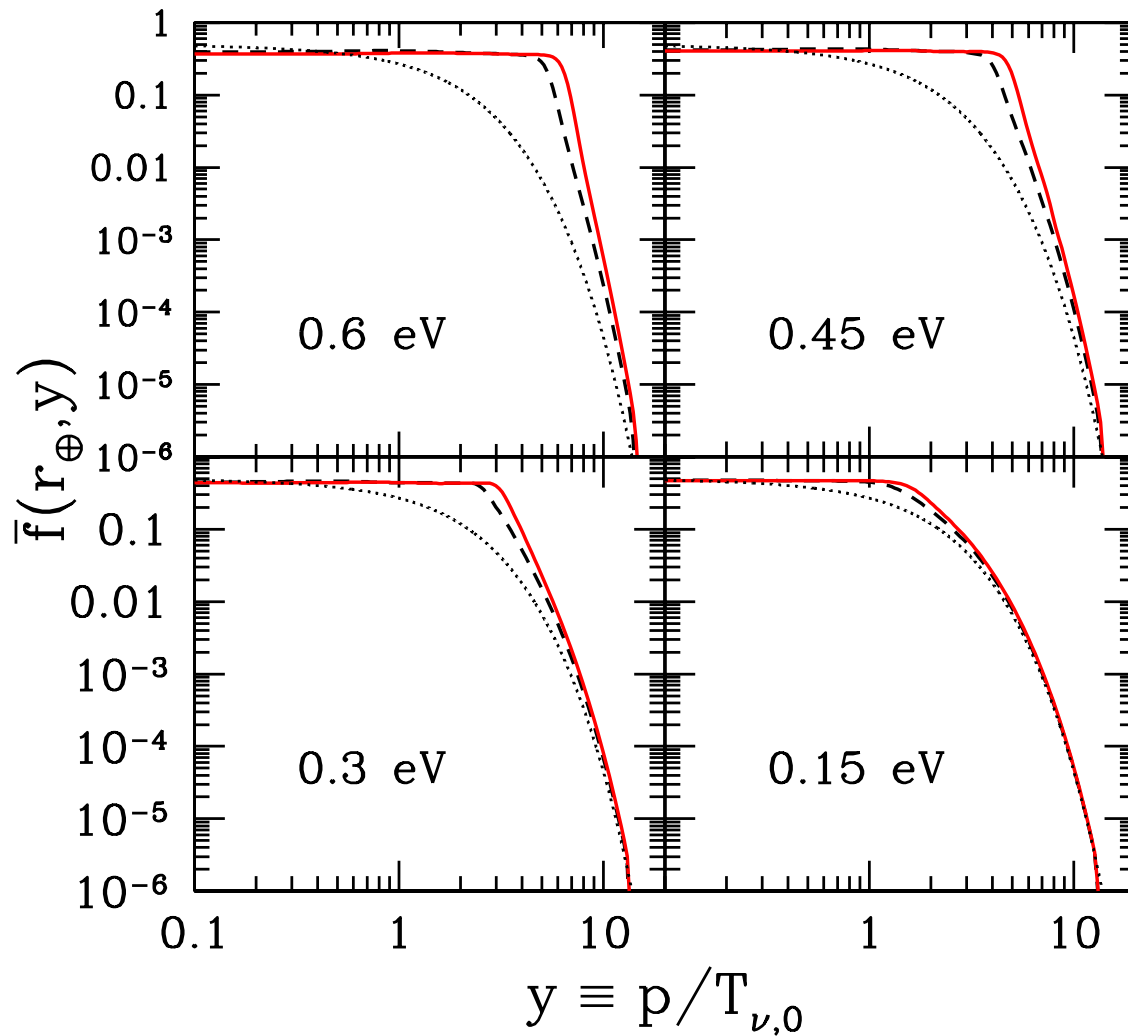


**Figure 6.** Momentum distribution of relic neutrinos at  $r_{\oplus}$  for various neutrino masses. The red (solid) line denotes the MWnow run, while the dashed line represents the NFWhalo run. The relativistic Fermi–Dirac function is indicated by the dotted line. The escape velocity  $v_{\text{esc}} = \sqrt{2|\phi(r_{\oplus})|}$  is  $490 \text{ km s}^{-1}$  and  $450 \text{ km s}^{-1}$  for MWnow and NFWhalo respectively, corresponding to “escape momenta”  $y_{\text{esc}} \equiv m_{\nu}v_{\text{esc}}/T_{\nu,0}$  of  $(5.9, 4.4, 3.0, 1.5)$  and  $(5.4, 4.1, 2.7, 1.4)$  for  $m_{\nu} = (0.6, 0.45, 0.3, 0.15) \text{ eV}$ .

bottom up, the mean momenta for the least clustered cases tend to be lower than the Fermi–Dirac value  $\langle p \rangle \simeq 3.15T_{\nu,0}$ , in contrast with the naïve expectation that clustering is necessarily accompanied by an increase in the neutrinos’ average kinetic energy.

### 7.3. Tremaine–Gunn bound

It is interesting to compare our results with nominal bounds from phase space arguments. By demanding the final coarse-grained distribution to be always less than the maximum of the original fine-grained distribution, Tremaine and Gunn [86] argued in 1979 that if neutrinos alone are to constitute the dark matter of a galactic halo, their mass must be larger than 20 eV, assuming that the halo has a Maxwellian phase space distribution as motivated by the theory of violent relaxation [85, 87, 88]. A modern version of this bound, in which the assumption about the phase space distribution is relaxed and which allows for contribution to the total gravitational potential from more than one form of matter, can be found in reference [89]. The revised mass bound may be written, alternatively, in the form of a constraint on the overdensity, which reads

$$\frac{n_\nu}{\bar{n}_\nu} < \frac{m_\nu^3 v_{\text{esc}}^3}{9\zeta(3)T_{\nu,0}^3}. \quad (7.3)$$

For the neutrino masses  $m_\nu = (0.6, 0.45, 0.3, 0.15)$  eV, this expression evaluates to  $(19, 8.0, 2.4, 0.3)$  and  $(15, 6.4, 1.8, 0.25)$  for MWnow and NFW halo, respectively, at  $r_\oplus$ .

At first sight, some of our numerical results seem to have completely violated the bound (7.3). But this cannot be, since we have seen explicitly that all of our final coarse-grained distributions satisfy perfectly the constraint  $\bar{f} \leq \max(f_0)$ . Furthermore, an upper bound of 0.25 on the overdensity for a 0.15 eV neutrino is obviously nonsensical.

The answer, as the astute reader would have figured, lies in accounting. In the derivation of (7.3), a semi-degenerate distribution has been summed only up to the momentum state corresponding to the escape velocity of the system. Neutrinos with higher momenta that could be hovering around in the vicinity have been completely ignored. In contrast, in our calculations, it is of no concern to us whether or not the relic neutrinos actually form bound states with the galaxy/halo. Therefore it is more appropriate for us to sum every neutrino in sight, rather than imposing a cut-off at  $v_{\text{esc}}$ . However, if we had imposed such a cut-off, one can easily see from Figure 6 that our overdensities would have just saturated the bound (7.3), so there is no conflict. Nonetheless, this illustrates how nominal bounds such as (7.3) must be used with care.

Before we conclude this section, let us note that for an NFW halo, the bound (7.3) can be written as

$$\begin{aligned} \frac{n_\nu}{\bar{n}_\nu} &< \frac{m_\nu^3}{9\zeta(3)T_{\nu,0}^3} \left[ \frac{2GM_{\text{vir}}}{g(c)} \frac{\ln(1+r/r_s)}{r} \right]^{3/2} \\ &\simeq 0.58 \times \left( \frac{m_\nu}{\text{eV}} \right)^3 \left[ \left( \frac{M_{\text{vir}}}{10^{12}h^{-1}M_\odot} \right) \left( \frac{h^{-1}\text{Mpc}}{r} \right) \frac{\ln(1+r/r_s)}{g(c)} \right]^{3/2}, \end{aligned} \quad (7.4)$$

where the function  $g(c)$  is defined in equation (A.8) in the Appendix. Figure 7 shows the bound as a function of radius for the various halo and neutrino masses considered

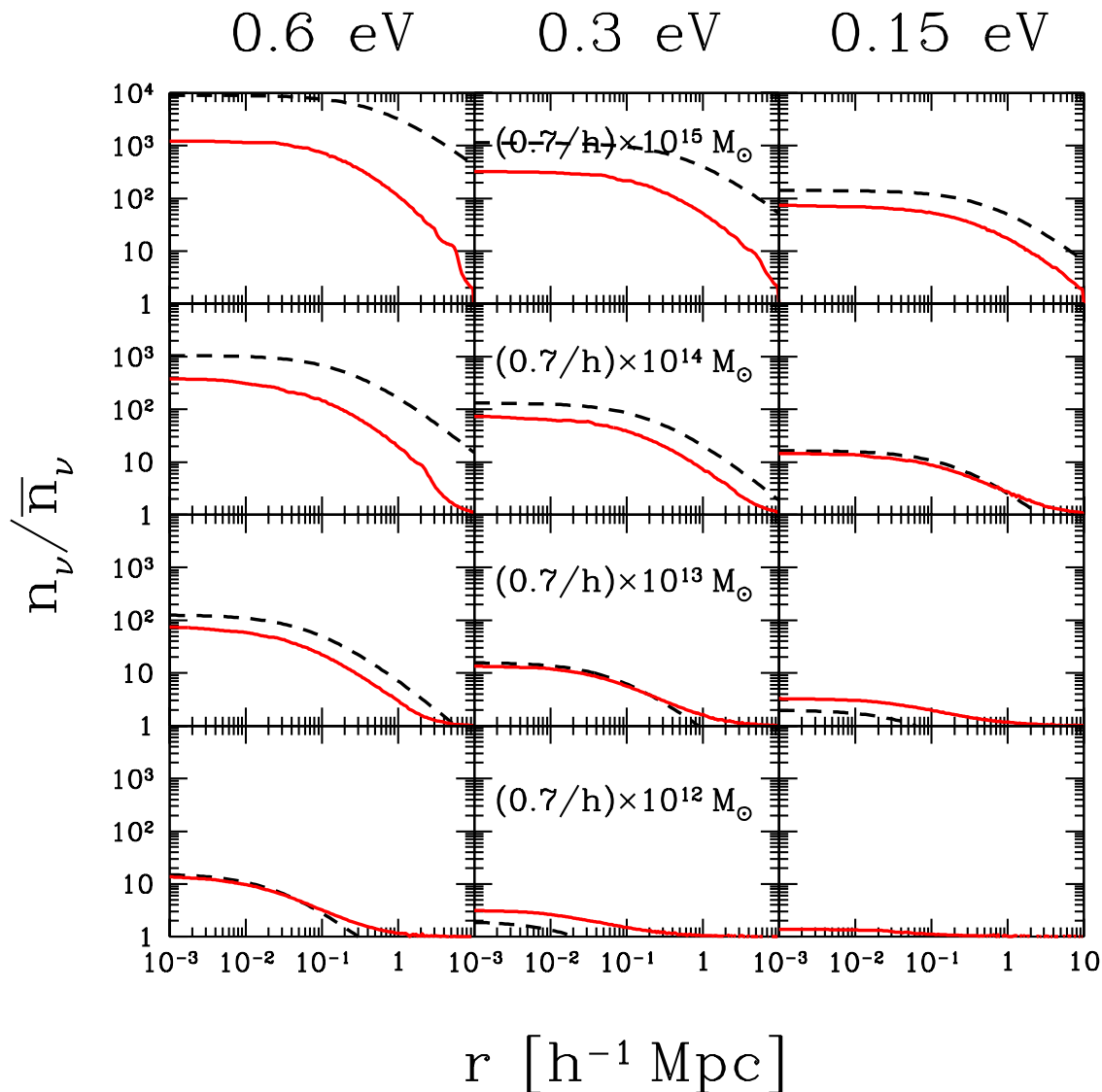


**Figure 7.** The Tremaine–Gunn bound on the neutrino overdensity for various halo and neutrino masses (dashed lines). The red (solid) lines correspond to our  $N$ -1-body results from section 5.

in section 5, along with the overdensities obtained from  $N$ -1-body simulations. We find the limit (7.3) to be saturated for the lightest halo and neutrino masses (and also some apparent violation of the bound due to different accounting). This explains why some of the overdensities exhibit an almost  $m_\nu^3$  dependence (cf. Figure 4). On the other hand, the heaviest  $\{m_\nu, M_{\text{vir}}\}$  set is short of the bound by at least one order of magnitude. This is also consistent with expectations: heavier halo and neutrino masses give a higher escape momentum  $p_{\text{esc}}$ , and higher momentum states are more difficult to fill up to a semi-degenerate level, since there are less particles in these states in the

original Fermi–Dirac distribution to begin with.

## 8. Implications for detection

In this section, we determine the implications of our clustering results for the direct detection of relic neutrinos, in contrast with the purely cosmological inferences discussed in section 2. We consider various proposed detection methods based on scattering processes, involving the relic neutrinos both as a beam and as a target. In particular, we shall discuss (i) coherent elastic scattering of the relic neutrino flux off target matter in a terrestrial detector (section 8.1), as well as (ii) the scattering of extremely energetic particles (accelerator beams or cosmic rays) off the relic neutrinos as a target (section 8.2).

### 8.1. Flux detection

The low average momentum  $\langle p \rangle = \langle y \rangle T_{\nu,0}$  of the relic neutrinos (cf. Table 2) corresponds to a (reduced) de Broglie wavelength of macroscopic dimension,  $\lambda = 1/\langle p \rangle = 0.12 \text{ cm}/\langle y \rangle$  (cf. Table 3). Therefore, one may envisage scattering processes in which many target atoms act coherently [4, 5] over a macroscopic volume  $\lambda^3$ , so that the reaction rate for elastic scattering becomes proportional to the square of the number of target atoms in that volume. Compared to the case where the neutrinos are elastically scattered coherently only on the individual nuclei of the target, the rate in this case is enhanced by a huge factor of

$$\frac{N_A}{A} \rho_t \lambda^3 \simeq 6 \times 10^{18} \left( \frac{100}{A} \right) \left( \frac{\rho_t}{\text{g/cm}^3} \right) \left( \frac{\lambda}{0.1 \text{ cm}} \right)^3, \quad (8.1)$$

where  $N_A$  is the Avogadro constant,  $A$  is the atomic mass, and  $\rho_t$  is the mass density of the target material.<sup>+</sup>

By exploiting the above coherence effect, a practical detection scheme for the local relic neutrino flux is based on the fact that a test body of density  $\rho_t$  at Earth will experience a neutrino wind force through random neutrino scattering events, leading to an acceleration [4, 5, 6, 93]

$$\begin{aligned} a_t &\simeq \sum_{\nu, \bar{\nu}} \underbrace{n_\nu v_{\text{rel}}}_{\text{flux}} \frac{4\pi}{3} N_A^2 \rho_t r_t^3 \underbrace{\sigma_{\nu N}}_{\text{mom. transfer}} \frac{2 m_\nu v_{\text{rel}}}{\hbar/(m_\nu v_{\text{rel}})} \\ &\simeq 2 \times 10^{-28} \left( \frac{n_\nu}{\bar{n}_\nu} \right) \left( \frac{10^{-3} c}{v_{\text{rel}}} \right) \left( \frac{\rho_t}{\text{g/cm}^3} \right) \left( \frac{r_t}{\hbar/(m_\nu v_{\text{rel}})} \right)^3 \text{ cm s}^{-2}, \quad (8.2) \end{aligned}$$

where  $\sigma_{\nu N} \simeq G_F^2 m_\nu^2/\pi$  is the elastic neutrino–nucleon cross section, and  $v_{\text{rel}} = \langle |\mathbf{v} - \mathbf{v}_\oplus| \rangle$  is the mean velocity of the relic neutrinos in the rest system of the detector. Here,  $v_\oplus \simeq 2.3 \times 10^2 \text{ km s}^{-1} \simeq 7.7 \times 10^{-4} c$  denotes the velocity of the Earth through the

<sup>+</sup> In the case of coherent scattering, it is possible, in principle, to measure also the scattering amplitude itself [90, 91, 92], which is linear in the Fermi coupling constant  $G_F$ . However, one needs a large lepton asymmetry for a non-negligible effect.

**Table 3.** Properties of the relic neutrinos at  $r_{\oplus}$  for various neutrino masses from the MWnow and NFWhalo runs (see text for definitions) relevant for their direct detection. The first column shows the overdensities. Columns two, three and four show, respectively, the mean absolute momenta, the associated mean reduced de Broglie wavelengths and the mean absolute velocities (in units of  $c$ ). The corresponding values for a relativistic Fermi–Dirac distribution are displayed in row one.

	$\frac{n_{\nu}}{\bar{n}_{\nu}}$	$\langle p \rangle$	$\lambda = \frac{\hbar}{\langle p \rangle}$	$\langle v \rangle$
Relativistic Fermi–Dirac	1	$5.3 \times 10^{-4}$ eV	$3.7 \times 10^{-2}$ cm	see (4.1)
NFWhalo, $m_{\nu} = 0.6$ eV	12	$7.2 \times 10^{-4}$ eV	$2.7 \times 10^{-2}$ cm	$1.2 \times 10^{-3}$
NFWhalo, $m_{\nu} = 0.45$ eV	6.4	$5.9 \times 10^{-4}$ eV	$3.4 \times 10^{-2}$ cm	$1.3 \times 10^{-3}$
NFWhalo, $m_{\nu} = 0.3$ eV	3.1	$5.0 \times 10^{-4}$ eV	$3.9 \times 10^{-2}$ cm	$1.7 \times 10^{-3}$
NFWhalo, $m_{\nu} = 0.15$ eV	1.4	$3.4 \times 10^{-4}$ eV	$5.9 \times 10^{-2}$ cm	$2.2 \times 10^{-3}$
MWnow, $m_{\nu} = 0.6$ eV	20	$8.5 \times 10^{-4}$ eV	$2.3 \times 10^{-2}$ cm	$1.4 \times 10^{-3}$
MWnow, $m_{\nu} = 0.45$ eV	10	$6.7 \times 10^{-4}$ eV	$2.9 \times 10^{-2}$ cm	$1.5 \times 10^{-3}$
MWnow, $m_{\nu} = 0.3$ eV	4.4	$5.4 \times 10^{-4}$ eV	$3.7 \times 10^{-2}$ cm	$1.8 \times 10^{-3}$
MWnow, $m_{\nu} = 0.15$ eV	1.6	$4.9 \times 10^{-4}$ eV	$4.1 \times 10^{-2}$ cm	$3.2 \times 10^{-3}$

Milky Way. Expression (8.2) is valid as long as the radius  $r_t$  of the target is smaller than the reduced de Broglie wavelength  $\lambda = \hbar/(m_{\nu}v_{\text{rel}})$  of the relic neutrinos. Furthermore, it applies only to Dirac neutrinos. For Majorana neutrinos, the acceleration is suppressed, in comparison with (8.2), by a factor of  $(v_{\text{rel}}/c)^2 \simeq 10^{-6}$  for an unpolarised target, or  $v_{\text{rel}}/c \simeq 10^{-3}$  for a polarised one. A target size much larger than  $\lambda$  can be exploited, while avoiding destructive interference, by using foam-like [4] or laminated [5] materials. Alternatively, grains of size  $\sim \lambda$  could be randomly embedded (with spacing  $\sim \lambda$ ) in a low density host material [94, 95].

To digest these estimates, we note that the smallest measurable acceleration at present is  $\gtrsim 10^{-13}$  cm s $^{-2}$ , using conventional Cavendish-type torsion balances. Possible improvements with currently available technology to a sensitivity of  $\gtrsim 10^{-23}$  cm s $^{-2}$  have been proposed [96, 97]. However, such a sensitivity is still off the prediction (8.2) by at least three orders of magnitude, as an inspection of the currently allowed range of local relic neutrino overdensities in Table 3 reveals. Therefore, we conclude that an observation of this effect will not be possible within the upcoming decade, but can still be envisaged in the foreseeable future (thirty to forty years according to reference [95], exploiting advances in nanotechnology), as long as our known light neutrinos are Dirac particles. Should they turn out, in the meantime, to be Majorana particles, flux detection via mechanical forces will be a real challenge.

Let us note finally that the background contribution to the acceleration (8.2) from the solar  $pp$  neutrinos [flux  $\sim 10^{11}$  cm $^{-2}$ s $^{-1}$ ,  $\langle E_{\nu} \rangle \sim 0.3$  MeV (e.g., [98]),  $a_t^{\nu \text{sun}} \simeq 10^{-27}$  cm s $^{-2}$  [6], may be rejected by directionality. The background from weakly interacting massive particles (WIMPs  $\chi$ , with mass  $m_{\chi}$ ) [6],

$$a_t^{\text{WIMP}} \simeq \underbrace{n_{\chi} v_{\text{rel}}}_{\text{flux}} N_A A \sigma_{\chi N} \underbrace{2 m_{\chi} v_{\text{rel}}}_{\text{mom. transfer}} \quad (8.3)$$

**Table 4.** Beam parameters of forthcoming accelerators and expected interaction rates with relic neutrinos.

accelerator	$N$	$A$	$Z$	$E_N$ [TeV]	$L$ [km]	$I$ [A]	$\left\  \frac{R_{\nu A}}{\left[ \frac{n_{\nu}}{n_{\nu}} \frac{m_{\nu}}{\text{eV}} \right]} \right\ $
LHC	$p$	1	1	7	26.7	$5.8 \times 10^{-1}$	$2 \times 10^{-8} \text{ yr}^{-1}$
	Pb	208	82	574	26.7	$6.1 \times 10^{-3}$	$1 \times 10^{-5} \text{ yr}^{-1}$
VLHC	$p$	1	1	87.5	233	$5.7 \times 10^{-2}$	$2 \times 10^{-7} \text{ yr}^{-1}$
	Pb	208	82	7280	233	$5.7 \times 10^{-4}$	$1 \times 10^{-4} \text{ yr}^{-1}$
ULHC	$p$	1	1	$10^7$	$4 \times 10^4$	$1.0 \times 10^{-1}$	$10 \text{ yr}^{-1}$

$$\simeq 6 \times 10^{-29} \left( \frac{\rho_{\chi}}{0.3 \text{ GeV/cm}^3} \right) \left( \frac{v_{\text{rel}}}{10^{-3} c} \right)^2 \left( \frac{A}{100} \right) \left( \frac{\sigma_{\chi N}}{10^{-45} \text{ cm}^2} \right) \text{ cm s}^{-2},$$

should they be the main constituent of the galactic dark matter with mass density  $\rho_{\chi} \equiv n_{\chi} m_{\chi} \simeq 0.3 \text{ GeV cm}^{-3}$  at  $r_{\oplus}$ , can be neglected as soon as the WIMP–nucleon cross section  $\sigma_{\chi N}$  is smaller than  $\sim 3 \times 10^{-45} \text{ cm}^2$ . This should be well established by the time relic neutrino direct detection becomes a reality. Note also that neutrinos produced in the Earth’s atmosphere do not contribute appreciably to  $a_t$  because of their small flux; for  $E_{\nu} \sim 0.1 \rightarrow 10 \text{ GeV}$ , the integrated flux is  $\lesssim 1 \text{ cm}^{-2} \text{ s}^{-1}$  (e.g., [99]).

## 8.2. Target detection

Let us consider next the idea to take advantage of the fact that, for center-of-mass (c.m.) energies below the  $W$ - and  $Z$ -resonances, the weak interaction cross sections grow rapidly with energy. One may then contemplate the possibility to exploit a flux of extremely energetic particles—either from accelerator beams or from cosmic rays—for scattering on the relic neutrinos.

*8.2.1. At accelerators* We start with a discussion of the prospects to detect interactions with the relic neutrinos at forthcoming accelerator beams such as the LHC [100] and the VLHC [101], with beam energies  $E_N$  ranging from 7 TeV for the LHC running with protons, up to several thousands of TeV for the heavy ion option at the VLHC (cf. Table 4). At these beams, the attainable momentum transfers and c.m. energies,

$$\sqrt{s} = \sqrt{2 m_{\nu} E_N} \simeq 4.5 \left( \frac{m_{\nu}}{\text{eV}} \right)^{1/2} \left( \frac{E_N}{10 \text{ TeV}} \right)^{1/2} \text{ MeV}, \quad (8.4)$$

are so small that the cross sections for their interactions with the relic neutrinos are enhanced by a factor  $\sim A^2$  due to coherent elastic scattering over the size of the nucleus [102], and grow linearly with the beam energy,

$$\sigma_{\nu \frac{A}{Z} N} \simeq A^2 G_F^2 s / \pi \simeq 3.4 \times 10^{-43} A^2 \left( \frac{m_{\nu}}{\text{eV}} \right) \left( \frac{E_N}{10 \text{ TeV}} \right) \text{ cm}^2. \quad (8.5)$$

This leads to a scattering rate [103, 104, 105]

$$\begin{aligned}
 R_{\nu \frac{A}{Z}N} &\simeq \sum_{\nu, \bar{\nu}} n_{\nu} \sigma_{\nu \frac{A}{Z}N} L I / (Z e) \\
 &\simeq 2 \times 10^{-8} \left( \frac{n_{\nu}}{\bar{n}_{\nu}} \right) \left( \frac{m_{\nu}}{\text{eV}} \right) \frac{A^2}{Z} \left( \frac{E_N}{10 \text{ TeV}} \right) \left( \frac{L}{100 \text{ km}} \right) \left( \frac{I}{0.1 \text{ A}} \right) \text{ yr}^{-1},
 \end{aligned}
 \tag{8.6}$$

for a beam of particles  $\frac{A}{Z}N$ , with charge  $Z e$ , length  $L$  and current  $I$ . In view of the currently allowed range of local relic neutrino overdensities displayed in Table 3, and the beam parameters of the next generation of accelerators summarised in Table 4, the expected rate (8.6) is clearly too small to give rise to an observable effect in the foreseeable future. The extremely energetic 574 TeV lead beam at the LHC will have less than  $10^{-4}$  interactions per year with relic neutrinos, for  $m_{\nu} \lesssim 0.6$  eV and, correspondingly,  $n_{\nu}/\bar{n}_{\nu} \lesssim 20$ . Even a lead acceleration option for the VLHC, with  $E_N \simeq 7280$  TeV (or, equivalently, 35 TeV per nucleon) and a current  $I \simeq 5.7 \times 10^{-4}$  A (a hundredth of the nominal current of the  $p$  running mode) will give less than  $10^{-3}$  events per year for the most optimistic neutrino mass scenario. Thus, there is little hope, in the foreseeable future, to detect relic neutrino using terrestrial accelerator beams.

Let us nevertheless dream about the far future, in which an Ultimate Large Hadron Collider (ULHC) exists and is able to accelerate protons to energies above  $10^7$  TeV\* in a ring of ultimate circumference  $L \simeq 4 \times 10^4$  km around the Earth, thus leading to an interaction rate of more than one event per year (cf. Table 4). Even under these most optimistic circumstances, is it possible to reliably detect these interactions? Clearly, elastic scattering of the beam particles with the relic neutrinos—one of the contributions to the rate (8.6)—will be next to impossible to detect because of the small momentum transfers involved ( $\sim 1$  GeV at  $E_N \sim 10^7$  TeV). A very promising alternative is to consider again a heavy ion beam, and to exploit the contribution of the inverse beta decay reaction,

$$\frac{A}{Z}N + \nu_e \rightarrow \frac{A}{Z+1}N + e^{-},
 \tag{8.7}$$

to the rate (8.6). This reaction changes the charge of the nucleus, causing it to follow an extraordinary trajectory and finally to exit the machine such that it becomes susceptible to detection [104, 109]. A detection of this reaction would also clearly demonstrate that a neutrino was involved in the scattering.

*8.2.2. With cosmic rays* In the meantime, until the ULHC has been constructed, target detection of the relic neutrinos has to rely on extremely energetic cosmic rays. In fact, cosmic rays with up energies up to  $E_{\text{cr}} \sim 10^{20}$  eV have been seen by air shower

\* Note that a collider at this energy has to be built anyhow if one wishes to explore the “intermediate” scale  $(M_{\text{EW}} M_{\text{GUT}})^{1/2} \sim 10^{10}$  GeV between the electroweak scale  $M_{\text{EW}} \sim 1$  TeV and the scale of grand unification  $M_{\text{GUT}} \sim 10^{17}$  GeV. The intermediate scale is exploited in many schemes of supersymmetry breaking (e.g., [106]) and in seesaw mechanisms for neutrino masses [107, 108].

observatories. The corresponding c.m. energies are

$$\sqrt{s} = \sqrt{2 m_\nu E_{\text{cr}}} \simeq 14 \left( \frac{m_\nu}{\text{eV}} \right)^{1/2} \left( \frac{E_{\text{cr}}}{10^{20} \text{ eV}} \right)^{1/2} \text{ GeV} \quad (8.8)$$

when scattering off the relic neutrinos. These energies are not too far from the  $W$ - and  $Z$ -resonances, at which the electroweak cross sections become sizeable. Indeed, it was pointed out long ago by Weiler [7, 8] (for earlier suggestions, see [110, 111, 112, 113, 114]) that the resonant annihilation of extremely energetic cosmic neutrinos ( $\text{EEC}\nu$ ) with relic anti-neutrinos (and vice versa) into  $Z$ -bosons appears to be a unique process having sensitivity to the relic neutrinos. On resonance,

$$E_\nu^{\text{res}} = \frac{m_Z^2}{2m_\nu} \simeq 4 \times 10^{21} \left( \frac{\text{eV}}{m_\nu} \right) \text{ eV}, \quad (8.9)$$

the associated cross section is enhanced by several orders of magnitude,

$$\langle \sigma_{\text{ann}} \rangle = \int ds / m_Z^2 \sigma_{\nu\bar{\nu}}^Z(s) \simeq 2\pi\sqrt{2} G_F \simeq 4 \times 10^{-32} \text{ cm}^2, \quad (8.10)$$

leading to a “short” mean free path  $\ell_\nu = (\bar{n}_\nu \langle \sigma_{\text{ann}} \rangle)^{-1} \simeq 1.4 \times 10^5 \text{ Mpc}$  which is *only* about  $48 h$  times the Hubble distance. Neglecting cosmic evolution effects, this corresponds to an annihilation probability for  $\text{EEC}\nu$  from cosmological distances on the relic neutrinos of  $2 h^{-1}\%$ .

The signatures of annihilation are (i) absorption dips [7, 8, 9] (see also [115, 116, 117]) in the  $\text{EEC}\nu$  spectrum at the resonant energies, and (ii) emission features [10, 11, 12, 13, 14] ( $Z$ -bursts) as protons (or photons) with energies spanning a decade or more above the predicted Greisen–Zatsepin–Kuzmin (GZK) cutoff at  $E_{\text{GZK}} \simeq 4 \times 10^{19} \text{ eV}$  [118, 119]. This is the energy beyond which the CMB is absorbing to nucleons due to resonant photopion production.‡

The possibility to confirm the existence of relic neutrinos within the next decade from a measurement of the aforementioned absorption dips in the  $\text{EEC}\nu$  flux was recently investigated in [9]. Presently planned neutrino detectors (Pierre Auger Observatory [124], IceCube [125], ANITA [126], EUSO [127], OWL [128], and SalSA [129]) operating in the energy regime above  $10^{21} \text{ eV}$  appear to be sensitive enough to lead us, within the next decade, into an era of relic neutrino absorption spectroscopy, provided that the flux of the  $\text{EEC}\nu$  at the resonant energies is close to current observational bounds and the neutrino mass is sufficiently large,  $m_\nu \gtrsim 0.1 \text{ eV}$ . In this case, the associated  $Z$ -bursts must also be seen as post-GZK events at the planned cosmic ray detectors (Pierre Auger Observatory, EUSO, and OWL).

What are the implications of relic neutrino clustering for absorption and emission spectroscopy? Firstly, absorption spectroscopy is predominantly sensitive to the relic neutrino background at early times, with the depths of the absorption dips determined largely by the higher number densities at large redshifts ( $z \gg 1$ ). Since neutrinos do not cluster significantly until after  $z \lesssim 2$ , clustering at recent times can only show up as

‡ The association of  $Z$ -bursts with the mysterious cosmic rays observed above  $E_{\text{GZK}}$  is a controversial possibility [10, 11, 12, 13, 14, 120, 121, 122, 123].

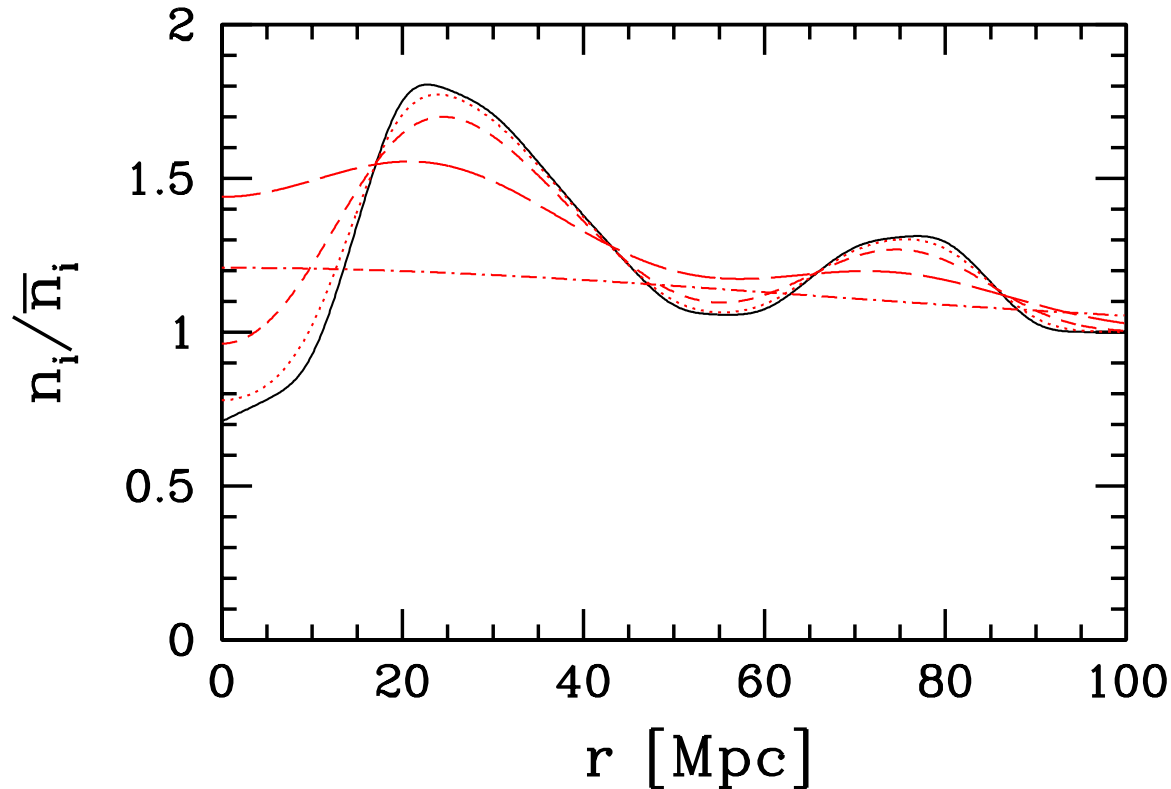


**Figure 8.** “Large scale” overdensities ( $i = \nu, \text{CDM}$ ) in the local universe, with the Milky Way at the origin, estimated from equation (6.18) assuming the function  $K(\mathbf{x})$  to be a Gaussian. The black (solid) line corresponds to the local CDM distribution inferred from peculiar velocity measurements [131] (see also [132]) smeared over the surface of a sphere with radius  $r$  [14]. The dotted line is the neutrino overdensity for  $m_\nu = 0.6$  eV, short dash 0.3 eV, long dash 0.15 eV, and dot-dash 0.04 eV.

secondary dips with such minimal widths in energy [130] that they do not seem likely to be resolved by planned observatories.

On the other hand, emission spectroscopy is directly sensitive to the relic neutrino content of the local universe ( $z \lesssim 0.01 \Leftrightarrow r_{\text{GZK}} \lesssim 50$  Mpc). However, since the neutrino density contrasts approximately track those of the underlying CDM above the neutrino free-streaming scale  $k_{\text{fs}}^{-1}$  (cf. section 6), it is clear that there cannot be a substantial neutrino overdensity over the whole GZK volume ( $\sim r_{\text{GZK}}^3$ ). Indeed, if we take the linear fitting formula (6.18), and apply it to the local CDM distribution inferred from peculiar velocity measurements (with a  $\sim 5$  Mpc smoothing), one can see in Figure 8 that the estimated neutrino overdensity is always  $\lesssim 2$ . Hence the overall emission rate cannot be significantly enhanced by gravitational clustering.

Or we could imagine doing “relic neutrino tomography” of the local universe, by exploiting the fact that there are several galaxy clusters ( $\gtrsim 10^{14} M_\odot$ ), such as Virgo

(distance  $\sim 15$  Mpc) and Centaurus ( $\sim 45$  Mpc), within the GZK zone with significant neutrino clustering (cf. Figure 1). One could conceivably search for directional dependences in the emission events as a signature of  $\text{EEC}\nu$  annihilating on relic anti-neutrinos (and vice versa). For example, AGASA has an angular resolution of  $\sim 2^\circ$  [133]. This is already sufficient to resolve the internal structures of, say, the Virgo cluster (distance  $\sim 15$  Mpc,  $M_{\text{vir}} \sim 8 \times 10^{14} M_\odot$ ) which spans some  $10^\circ$  across the sky. Using our  $N$ -1-body clustering results in Figure 1, the average neutrino overdensity along the line of sight towards and up to Virgo is estimated to be  $\sim 45$  and  $\sim 5$  for  $m_\nu = 0.6$  eV and 0.15 eV respectively, given an angular resolution of  $\sim 2^\circ$ . The corresponding increases in the number of events coming from the direction of the Virgo cluster relative to the unclustered case, assuming an isotropic distribution of  $\text{EEC}\nu$  sources, are given roughly by the same numbers, since protons originating from  $\sim 15$  Mpc away arrive at Earth approximately unattenuated. The numbers improve to  $\sim 55$  and  $\sim 8$  respectively with a finer  $\sim 1^\circ$  angular resolution.

Note that our estimates here are generally a factor of few higher than the predictions of SM. This is expected, because the linear method adopted in their analysis cannot account for additional clustering from nonlinear effects, as we demonstrated in section 6.

## 9. Conclusion

We have conducted a systematic and exhaustive study of the gravitational clustering of big bang relic neutrinos onto existing CDM and baryonic structures within the flat  $\Lambda$ CDM model, with the aim of understanding their clustering properties on galactic and sub-galactic scales for the purpose of designing possible scattering-based detection methods. Our main computational tools are (i) a restricted,  $N$ -1-body method (section 5), in which we neglect the gravitational interaction between the neutrinos and treat them as test particles moving in an external potential generated by the CDM/baryonic structures, and (ii) a semi-analytical, linear technique (section 6), which requires additional assumptions about the neutrino phase space distribution. In both cases, the CDM/baryonic gravitational potentials are calculated from parametric halo density profiles from high resolution  $N$ -body studies [60, 61] (section 4) and/or from realistic mass distributions reconstructed from observational data (e.g., [84, 131]).

Using these two computational techniques, we track the relic neutrinos' accretion onto CDM halos ranging from the galaxy to the galaxy cluster variety ( $M_{\text{vir}} \sim 10^{12} \rightarrow 10^{15} M_\odot$ ), and determine the neutrino number densities on scales  $\sim 1 \rightarrow 1000$  kpc for neutrino masses satisfying current constraints (2.1) from CMB and LSS (Figures 1 and 2). Because we can simulate only a finite set of halo and neutrino parameters, we provide also additional plots illustrating the approximate dependences of the neutrino overdensities on the halo and neutrino masses (Figures 3 and 4). These can be used for interpolation between simulation results. Furthermore, we find that the linear technique systematically underestimates the neutrino overdensities over the whole range of halo and neutrino masses considered in this study (Figure 1). Reconciliation with  $N$ -1-body

simulations can only be achieved if we impose a smoothing scale of  $\gtrsim 1$  Mpc, or if the overdensity is no more than three or four. We therefore conclude that the linear theory does not generally constitute a faithful approximation to the Vlasov equation in the study of neutrino clustering on galactic and sub-galactic scales ( $\lesssim 50$  kpc). However, it may still be useful for finding the minimum effects of neutrino clustering in other contexts not considered in this work (e.g., the nonlinear matter power spectrum [134]).

Next we apply our  $N$ -1-body method to calculate the relic neutrino number density in the Milky Way (section 7), especially their phase space distribution in our local neighbourhood at Earth  $r_{\oplus}$ , taking also into account contributions to the total gravitational potential from the galactic bulge and disk. We find a maximum overdensity of  $\sim 20$  per neutrino flavour in our immediate vicinity, provided that the neutrino mass is at its current upper limit of 0.6 eV (Table 2 and Figure 5). For neutrino masses less than 0.15 eV, the expected overdensity from gravitational clustering is less than two. The associated coarse-grained momentum spectra show varying degrees of deviation from the relativistic Fermi–Dirac function, but share a common feature that they are semi-degenerate, with phase space density  $\bar{f} \sim 1/2$ , up to the momentum state corresponding to the escape velocity from the Milky Way at  $r_{\oplus}$  (Figure 6). This means that the neutrino number densities we have calculated here for  $r_{\oplus}$  are already the *highest possible*, given the neutrino mass, without violating phase space constraints (e.g., [85, 89]). In order to attain even higher densities, one must now appeal to non-standard theories (e.g., [135]).

In terms of scattering-based detection possibilities, this meager enhancement in the neutrino number density in the Milky Way from gravitational clustering means that relic neutrinos are still far from being detected in fully earthbound laboratory experiments. For flux detection methods based on coherent elastic scattering of relic neutrinos off target matter in a terrestrial detector (section 8.1), a positive detection could be thirty to forty years away [95], provided that light neutrinos are Dirac particles. For light Majorana neutrinos, another  $\sim 10^3$  times more sensitivity would be required in the detector for a positive signal. Target detection methods using accelerator beams (section 8.2.1) seem equally hopeless, unless the accelerator is the size of the Earth and operates at an energy of  $\sim 10^7$  TeV (Table 4).

Meanwhile, target detection using extremely energetic cosmic neutrinos (EEC $\nu$ ,  $\gtrsim 10^{21}$  eV) remains the only viable means to confirm the existence of big bang relic neutrinos within the next decade or so (section 8.2.2). Resonant annihilation of EEC $\nu$  on relic neutrinos can be revealed as absorption dips in the EEC $\nu$  flux (e.g., [9]), or as emission features in the  $Z$ -decay products. However, since absorption spectroscopy is largely insensitive to late time ( $z \lesssim 2$ ) relic neutrino clustering, our findings here have little impact on the conclusions of [9]. On the other hand, emission spectroscopy is sensitive to the relic neutrino content of the local GZK zone,  $V_{\text{GZK}} \sim 50^3$  Mpc $^3$ . While we find no significant large scale clustering within  $V_{\text{GZK}}$  (Figure 8) and therefore no significant enhancement in the overall emission rates, it is still conceivable to exploit the considerable neutrino overdensities in nearby galaxy clusters, and search for directional dependences in the post-GZK emission events. For the Virgo cluster, for example,

we estimate the event rate from the central  $1^\circ$  region to be  $\sim 55$  and  $\sim 8$  times the unclustered rate for neutrino mass  $m_\nu = 0.6$  eV and  $0.15$  eV respectively, assuming an isotropic distribution of EEC $\nu$  sources. [Our estimates differ by a factor of a few from the predictions of [25] because their linear technique fails to account for additional clustering from nonlinear effects, as we have demonstrated in this study (section 6)]. Planned observatories such as the Pierre Auger Observatory [124], EUSO [127] and OWL [128] will have sufficient angular resolution to, in principle, see this enhancement. However, considering the rapidly improving constraints on both the EEC $\nu$  flux and neutrino masses, it remains to be seen if the enhancement can indeed be observed with enough statistical significance.

## Acknowledgments

We would like to thank David Cerdeño, Pasquale Di Bari, Birgit Eberle, Jan Hamann, Oleg Lebedev, Helmut Mais, and Thomas Reiter for useful discussions.

## Appendix A. Details of $N$ -1-body simulations

We give in this appendix a detailed discussion of the techniques used in our  $N$ -1-body simulations.

### Appendix A.1. Hamilton's equations

Following [59], we begin with a Lagrangian  $L(\mathbf{x}, \dot{\mathbf{x}}, \tau) = a \left[ \frac{1}{2} m_\nu v^2 - m_\nu \phi(|\mathbf{x}|, \tau) \right]$  for a test particle (neutrino) with mass  $m_\nu$  and peculiar velocity  $\mathbf{v} \equiv \dot{\mathbf{x}}$  moving in a spherically symmetric gravitational potential well  $\phi(\mathbf{x}, \tau)$  generated by the CDM halo. Because of spherical symmetry, the motion of the test particle is confined to a plane. This allows us to switch to polar coordinates  $\{r, \theta\}$  to obtain

$$L(r, \theta, \dot{r}, \dot{\theta}, \tau) = a \left[ \frac{1}{2} m_\nu (\dot{r}^2 + r^2 \dot{\theta}^2) - m_\nu \phi(r, \tau) \right], \quad (\text{A.1})$$

and eliminate two superfluous variables in the process. The canonical momenta conjugate to  $r$  and  $\theta$  are  $p_r \equiv \partial L / \partial \dot{r} = am_\nu \dot{r}$  and  $\ell \equiv r p_\theta \equiv \partial L / \partial \dot{\theta} = am_\nu r^2 \dot{\theta}$  respectively, leading to the Hamiltonian

$$H(r, \theta, p_r, \ell, \tau) = \frac{1}{2am_\nu} \left[ p_r^2 + \frac{\ell^2}{r^2} \right] + am_\nu \phi(r, \tau), \quad (\text{A.2})$$

and hence Hamilton's equations

$$\begin{aligned} \frac{dr}{d\tau} &= \frac{p_r}{am_\nu}, & \frac{d\theta}{d\tau} &= \frac{\ell}{am_\nu r^2}, \\ \frac{dp_r}{d\tau} &= \frac{\ell^2}{am_\nu r^3} - am_\nu \frac{\partial \phi}{\partial r}, & \frac{d\ell}{d\tau} &= 0, \end{aligned} \quad (\text{A.3})$$

where the last equality expresses the conservation of conjugate comoving angular momentum  $\ell$ .

For computational purposes, it is convenient to rewrite the set of differential equations (A.3) in terms of redshift  $z$  and the normalised quantities  $u_r \equiv p_r/m_\nu = a\dot{r}$  and  $u_\theta \equiv \ell/m_\nu = ar^2\dot{\theta}$ , thus rendering (A.3) into the form

$$\begin{aligned} \frac{dr}{dz} &= -\frac{u_r}{\dot{a}}, & \frac{d\theta}{dz} &= -\frac{u_\theta}{\dot{a}r^2}, \\ \frac{du_r}{dz} &= -\frac{1}{\dot{a}} \left( \frac{u_\theta^2}{r^3} - a^2 \frac{\partial\phi}{\partial r} \right), & \frac{du_\theta}{dz} &= 0, \end{aligned} \quad (\text{A.4})$$

where  $a = (1+z)^{-1}$  and  $\dot{a} = H_0 \sqrt{a^{-1} \Omega_{m,0} + a^2 \Omega_{\Lambda,0}}$  are, respectively, the scale factor and the expansion rate, the latter of which is determined by the present day Hubble constant  $H_0$  and the cosmological model in hand.

The gravitational potential  $\phi(r, \tau)$  obeys the Poisson equation

$$\nabla^2 \phi \rightarrow \frac{1}{r^2} \frac{\partial}{\partial r} \left( r^2 \frac{\partial\phi}{\partial r} \right) = 4\pi G a^2 \bar{\rho}_m(\tau) \delta_m(r, \tau). \quad (\text{A.5})$$

Since we are treating the CDM halo as a density perturbation sitting on top of a uniform background, i.e.,  $\bar{\rho}_m(\tau) \delta_m(r, \tau) \rightarrow \rho_{\text{halo}}(r)$ , we have the following (partial) solution:

$$\frac{\partial\phi}{\partial r} = \frac{4\pi G a^2}{r^2} \int_0^r \rho_{\text{halo}}(r', \tau) r'^2 dr' = \frac{G}{a r^2} M_{\text{halo}}(r), \quad (\text{A.6})$$

where  $M_{\text{halo}}(r)$  is the physical mass contained in a sphere of radius  $r$ . For an NFW halo,

$$M_{\text{halo}}(r) = 4\pi a^3 \rho_s r_s^3 g(x) = M_{\text{vir}} g(x) / g(c), \quad x = r/r_s, \quad (\text{A.7})$$

$$g(x) = \ln(1+x) - \frac{x}{1+x}, \quad (\text{A.8})$$

$$c = \frac{9}{1+z} \left( \frac{M_{\text{vir}}}{1.5 \times 10^{13} h^{-1} M_\odot} \right)^{-0.13}, \quad (\text{A.9})$$

$$\begin{aligned} r_s &= \frac{1}{c} \left( \frac{3}{4\pi \bar{\rho}_{m,0} \Delta_{\text{vir}}} M_{\text{vir}} \right)^{1/3} \\ &= 9.51 \times 10^{-1} c^{-1} \Omega_{m,0}^{-1/3} \Delta_{\text{vir}}^{-1/3} \left( \frac{M_{\text{vir}}}{10^{12} h^{-1} M_\odot} \right)^{1/3} h^{-1} \text{Mpc}. \end{aligned} \quad (\text{A.10})$$

The meanings of these various symbols are explained in section 4.

### Appendix A.2. Discretising the initial phase space distribution

The number of neutrinos at some initial time  $\tau_i$  in the interval  $(\mathbf{x}, \mathbf{p}) \rightarrow (\mathbf{x} + d\mathbf{x}, \mathbf{p} + d\mathbf{p})$  is defined to be

$$dN = f(\mathbf{x}, \mathbf{p}, \tau_i) d^3x d^3p. \quad (\text{A.11})$$

We assume the initial phase space distribution to be isotropic and homogeneous, i.e.,  $f(\mathbf{x}, \mathbf{p}, \tau_i) = f_0(p)$ . This initial homogeneity implies that the ensemble's subsequent evolution under a spherically symmetric potential will depend only on the initial radial distance  $r$ , radial momentum  $p_r$ , and transverse momentum  $p_T = \sqrt{p^2 - p_r^2}$ . Thus we may rewrite the phase space volume element as

$$d^3x \rightarrow r^2 \sin\theta d\theta d\phi dr, \quad d^3p \rightarrow p_T dp_T dp_r d\varphi, \quad (\text{A.12})$$

with  $r \in [0, \infty)$ ,  $\theta \in [0, \pi]$ ,  $\phi \in [0, 2\pi)$ , and  $p_T \in [0, \infty)$ ,  $p_r \in (-\infty, \infty)$ ,  $\varphi \in [0, 2\pi)$ .

In an ideal and perfectly deterministic calculation, one would track the motion of every particle for every occupied combination of  $r$ ,  $p_r$  and  $p_T$ . This is obviously impossible in practice; one must therefore resort to simulating only a representative set of particles and endow each with a ‘‘weight’’ according to the phase space region from which the particle is drawn. We show below how this weight is calculated.††

Suppose that a point particle initially at  $(r, p_r, p_T)$  is representative for all particles in the initial phase space interval  $(r_a, p_{r,a}, p_{T,a}) \rightarrow (r_b, p_{r,b}, p_{T,b})$ . The weight carried by this representative particle is defined as

$$w_i \equiv \int_{r_a, p_{r,a}, p_{T,a}}^{r_b, p_{r,b}, p_{T,b}} \int_{\theta, \phi, \varphi} dN, \quad (\text{A.13})$$

where  $\int_{\theta, \phi, \varphi}$  means summing over all  $\theta$ ,  $\phi$  and  $\varphi$ , which is simple:  $\int_{\theta, \phi, \varphi} \sin \theta d\theta d\phi d\varphi = 8\pi^2$ . The spatial integral over  $r$  is also readily calculable. The remaining phase space integral  $\int_{p_{r,a}, p_{T,a}}^{p_{r,b}, p_{T,b}} f(p) p_T dp_T dp_r$  can be solved by way of the parameterisation  $p_r = p \cos \psi$ , and  $p_T = p \sin \psi$ , and hence

$$p_T dp_T dp_r \rightarrow p^2 \sin \psi d\psi, \quad p \in [0, \infty), \psi \in [0, \pi). \quad (\text{A.14})$$

Thus the weight carried by a point particle centred on and representing the interval  $(r_a, p_a, \psi_a) \rightarrow (r_b, p_b, \psi_b)$  is given by

$$w_i = 8\pi^2 T_{\nu,0}^3 \int_{r_a}^{r_b} r^2 dr \int_{y_a}^{y_b} f(y) y^2 dy \int_{\psi_a}^{\psi_b} \sin \psi d\psi, \quad (\text{A.15})$$

where  $y = p/T_{\nu,0}$  is a dimensionless momentum variable.

### Appendix A.3. Kernel method for density profile estimation

We construct the neutrino density profiles from the discrete outputs of our  $N$ -1-body simulations using the kernel method of [65] and [70], which we reproduce here for completeness.

The number density corresponding to a set of particles is estimated to be

$$n(\mathbf{r}) = \sum_{i=1}^N \frac{w_i}{h^3} K \left[ \frac{1}{h} |\mathbf{r} - \mathbf{r}_i| \right], \quad (\text{A.16})$$

where  $w_i$  is the weight carried by the  $i$ th particle,  $h$  is the window width, and  $K$  is a normalised kernel such as the Gaussian kernel,

$$K(y) = \frac{1}{(2\pi)^{3/2}} e^{-y^2/2}. \quad (\text{A.17})$$

In order to obtain a spherically symmetric profile, we smear every particle around the surface of a sphere with radius  $r_i$  centred on  $r = 0$ . The spherically symmetric density estimate is then

$$n(r) = \sum_{i=1}^N \frac{w_i}{h^3} \tilde{K}(r, r_i, h), \quad (\text{A.18})$$

†† We note for completeness that the concept of super particles with equal masses or, in our language, weights is adopted in most full scale  $N$ -body simulations [15]. The representative point particles are drawn randomly from the initial phase space distribution.

with

$$\widetilde{K}(r, r_i, h) \equiv \frac{1}{4\pi} \int d\phi \int d\theta \sin\theta \widetilde{K} \left( h^{-1} \sqrt{r^2 + r_i^2 - 2rr_i \cos\theta} \right). \quad (\text{A.19})$$

Substituting for the Gaussian kernel, we get

$$\widetilde{K}(r, r_i, h) = \frac{1}{2(2\pi)^{3/2} rr_i} \frac{h^2}{h^2} \left[ e^{-(r-r_i)^2/2h^2} - e^{-(r+r_i)^2/2h^2} \right]. \quad (\text{A.20})$$

The optimal choice of  $h$  generally depends on the underlying function  $n(r)$  [70]. In our analysis, however, a constant  $h$  is adopted for simplicity. Our momentum distributions in section 7 are also constructed with this kernel method.

## References

- [1] S. Eidelman *et al.* [Particle Data Group Collaboration], Phys. Lett. B **592** (2004) 1.
- [2] S. Hannestad, New J. Phys. 6 (2004) **108** [arXiv:hep-ph/0404239].
- [3] G. L. Fogli, E. Lisi, A. Marrone, D. Montanino, A. Palazzo and A. M. Rotunno, eConf **C030626** (2003) THAT05 [arXiv:hep-ph/0310012].
- [4] B. F. Shvartsman, V. B. Braginsky, S. S. Gershtein, Y. B. Zeldovich and M. Y. Khlopov, JETP Lett. **36** (1982) 277 [Pisma Zh. Eksp. Teor. Fiz. **36** (1982) 224].
- [5] P. F. Smith and J. D. Lewin, Phys. Lett. B **127** (1983) 185.
- [6] G. Duda, G. Gelmini and S. Nussinov, Phys. Rev. D **64** (2001) 122001 [arXiv:hep-ph/0107027].
- [7] T. J. Weiler, Phys. Rev. Lett. **49** (1982) 234.
- [8] T. J. Weiler, Astrophys. J. **285** (1984) 495.
- [9] B. Eberle, A. Ringwald, L. Song and T. J. Weiler, Phys. Rev. D **70** (2004) 023007 [arXiv:hep-ph/0401203].
- [10] D. Fargion, B. Mele and A. Salis, Astrophys. J. **517** (1999) 725 [arXiv:astro-ph/9710029].
- [11] T. J. Weiler, Astropart. Phys. **11** (1999) 303 [arXiv:hep-ph/9710431].
- [12] S. Yoshida, G. Sigl and S. J. Lee, Phys. Rev. Lett. **81** (1998) 5505 [arXiv:hep-ph/9808324].
- [13] Z. Fodor, S. D. Katz and A. Ringwald, Phys. Rev. Lett. **88** (2002) 171101 [arXiv:hep-ph/0105064].
- [14] Z. Fodor, S. D. Katz and A. Ringwald, JHEP **0206** (2002) 046 [arXiv:hep-ph/0203198].
- [15] R. W. Hockney and J. W. Eastwood, *Computer Simulation Using Particles* (McGraw-Hill, New York, 1981).
- [16] G. Efstathiou, M. Davis, C. S. Frenk and S. D. M. White, Astrophys. J. Suppl. **57** (1985) 241.
- [17] E. Bertschinger, Ann. Rev. Astron. Astrophys. **36** (1998) 599.
- [18] A. Klypin, in *Modern Cosmology*, edited by S. Bonometto, V. Gorini, and U. Moschella (IOP, Bristol, 2002), p. 420.
- [19] C. P. Ma and E. Bertschinger, Astrophys. J. **434** (1994) L5 [arXiv:astro-ph/9407085].
- [20] Y. P. Jing and L. Z. Fang, Astrophys. J. **432** (1994) 438 [arXiv:astro-ph/9403012].
- [21] R. A. C. Croft and G. Efstathiou, Mon. Not. Roy. Astron. Soc. **268** (1994) L23.
- [22] C. Walter and A. Klypin, Astrophys. J. **462** (1996) 13 [arXiv:astro-ph/9507074].
- [23] L. Kofman, A. Klypin, D. Pogosian and J. P. Henry, Astrophys. J. **470** (1996) 102 [arXiv:astro-ph/9509145].
- [24] A. Blanchard, M. Douspis, M. Rowan-Robinson and S. Sarkar, Astron. Astrophys. **412** (2003) 35 [arXiv:astro-ph/0304237].
- [25] S. Singh and C. P. Ma, Phys. Rev. D **67** (2003) 023506 [arXiv:astro-ph/0208419].
- [26] J. A. Sellwood, Ann. Rev. Astron. Astrophys. **25** (1987) 151.
- [27] G. Abbiendi *et al.* [OPAL Collaboration], Eur. Phys. J. C **19** (2001) 587 [arXiv:hep-ex/0012018].
- [28] C. Weinheimer, Nucl. Phys. Proc. Suppl. **118** (2003) 279.
- [29] V. M. Lobashev *et al.*, Nucl. Phys. Proc. Suppl. **91** (2001) 280.
- [30] A. Osipowicz *et al.* [KATRIN Collaboration], arXiv:hep-ex/0109033.

- [31] M. Tegmark *et al.* [SDSS Collaboration], *Phys. Rev. D* **69** (2004) 103501 [arXiv:astro-ph/0310723].
- [32] G. L. Fogli, E. Lisi, A. Marrone, A. Melchiorri, A. Palazzo, P. Serra and J. Silk, arXiv:hep-ph/0408045.
- [33] S. Hannestad, *JCAP* **0305** (2003) 004 [arXiv:astro-ph/0303076].
- [34] C. L. Bennett *et al.*, *Astrophys. J. Suppl.* **148** (2003) 1 [arXiv:astro-ph/0302207].
- [35] M. Tegmark *et al.* [SDSS Collaboration], *Astrophys. J.* **606** (2004) 702 [arXiv:astro-ph/0310725].
- [36] J. A. Peacock *et al.*, *Nature* **410** (2001) 169 [arXiv:astro-ph/0103143].
- [37] W. L. Freedman *et al.*, *Astrophys. J.* **553** (2001) 47 [arXiv:astro-ph/0012376].
- [38] R. A. Knop *et al.*, *Astrophys. J.* **598** (2003) 102 [arXiv:astro-ph/0309368].
- [39] U. Seljak *et al.*, arXiv:astro-ph/0406594.
- [40] U. Seljak *et al.*, arXiv:astro-ph/0407372.
- [41] D. N. Spergel *et al.*, *Astrophys. J. Suppl.* **148** (2003) 175 [arXiv:astro-ph/0302209].
- [42] Ø. Elgarøy and O. Lahav, *JCAP* **0304** (2003) 004 [arXiv:astro-ph/0303089].
- [43] P. Crotty, J. Lesgourgues and S. Pastor, *Phys. Rev. D* **69** (2004) 123007 [arXiv:hep-ph/0402049].
- [44] V. Barger, D. Marfatia and A. Tregre, *Phys. Lett. B* **595** (2004) 55 [arXiv:hep-ph/0312065].
- [45] K. N. Abazajian and S. Dodelson, *Phys. Rev. Lett.* **91** (2003) 041301 [arXiv:astro-ph/0212216].
- [46] M. Kaplinghat, L. Knox and Y. S. Song, *Phys. Rev. Lett.* **91** (2003) 241301 [arXiv:astro-ph/0303344].
- [47] S. Hannestad and G. Raffelt, *JCAP* **0404** (2004) 008 [arXiv:hep-ph/0312154].
- [48] P. Crotty, J. Lesgourgues and S. Pastor, *Phys. Rev. D* **67** (2003) 123005 [arXiv:astro-ph/0302337].
- [49] E. Pierpaoli, *Mon. Not. Roy. Astron. Soc.* **342** (2003) L63 [arXiv:astro-ph/0302465].
- [50] V. Barger, J. P. Kneller, H. S. Lee, D. Marfatia and G. Steigman, *Phys. Lett. B* **566** (2003) 8 [arXiv:hep-ph/0305075].
- [51] R. Bowen, S. H. Hansen, A. Melchiorri, J. Silk and R. Trotta, *Mon. Not. Roy. Astron. Soc.* **334** (2002) 760 [arXiv:astro-ph/0110636].
- [52] S. Bashinsky and U. Seljak, *Phys. Rev. D* **69** (2004) 083002 [arXiv:astro-ph/0310198].
- [53] R. H. Cyburt, B. D. Fields, K. A. Olive and E. Skillman, arXiv:astro-ph/0408033.
- [54] A. Cuoco, F. Iocco, G. Mangano, G. Miele, O. Pisanti and P. D. Serpico, arXiv:astro-ph/0307213.
- [55] V. Barger, J. P. Kneller, P. Langacker, D. Marfatia and G. Steigman, *Phys. Lett. B* **569** (2003) 123 [arXiv:hep-ph/0306061].
- [56] A. D. Dolgov, S. H. Hansen, S. Pastor, S. T. Petcov, G. G. Raffelt and D. V. Semikoz, *Nucl. Phys. B* **632** (2002) 363 [arXiv:hep-ph/0201287].
- [57] Y. Y. Y. Wong, *Phys. Rev. D* **66** (2002) 025015 [arXiv:hep-ph/0203180].
- [58] K. N. Abazajian, J. F. Beacom and N. F. Bell, *Phys. Rev. D* **66** (2002) 013008 [arXiv:astro-ph/0203442].
- [59] E. Bertschinger, in *Les Houches Cosmology 1993*, pp. 273-348, arXiv:astro-ph/9503125.
- [60] J. F. Navarro, C. S. Frenk and S. D. M. White, *Astrophys. J.* **462** (1996) 563 [arXiv:astro-ph/9508025].
- [61] J. F. Navarro, C. S. Frenk and S. D. M. White, *Astrophys. J.* **490** (1997) 493.
- [62] A. V. Kravtsov, A. A. Klypin and A. M. Khokhlov, *Astrophys. J. Suppl.* **111** (1997) 73 [arXiv:astro-ph/9701195].
- [63] Y. P. Jing, *Astrophys. J.* **535** (2000) 30 [arXiv:astro-ph/9901340].
- [64] J. S. Bullock *et al.*, *Mon. Not. Roy. Astron. Soc.* **321** (2001) 559 [arXiv:astro-ph/9908159].
- [65] D. Reed *et al.*, *Mon. Not. Roy. Astron. Soc.* **346** (2003) 565 [arXiv:astro-ph/0312544].
- [66] B. Moore, T. Quinn, F. Governato, J. Stadel and G. Lake, *Mon. Not. Roy. Astron. Soc.* **310** (1999) 1147 [arXiv:astro-ph/9903164].
- [67] Y. P. Jing and Y. Suto, *Astrophys. J. Lett.* **529** (2000) L69 [arXiv:astro-ph/9909478].
- [68] C. P. Ma and J. N. Fry, *Astrophys. J.* **543** (2000) 503 [arXiv:astro-ph/0003343].
- [69] G. L. Bryan and M. L. Norman, *Astrophys. J.* **495** (1998) 80 [arXiv:astro-ph/9710107].
- [70] D. Merritt and B. Tremblay, *Astron. J.* **108** (1994) 514.
- [71] I. H. Gilbert, *Astrophys. J.* **144** (1966) 233.

- [72] J. R. Bond and A. S. Szalay, *Astrophys. J.* **274** (1983) 443.
- [73] R. H. Brandenberger, N. Kaiser and N. Turok, *Phys. Rev. D* **36** (1987) 2242.
- [74] E. Bertschinger and P. N. Watts, *Astrophys. J.* **328** (1988) 23.
- [75] L. Perivolaropoulos, R. H. Brandenberger and A. Stebbins, *Phys. Rev. D* **41** (1990) 1764.
- [76] S. Setayeshgar, SB thesis (MIT, 1990).
- [77] J. Binney and S. Tremaine, *Galactic Dynamics* (Princeton University Press, Princeton NJ, 1987)
- [78] S. D. M. White and M. J. Rees, *Mon. Not. Roy. Astro. Soc.* **183** (1978) 341.
- [79] G. R. Blumenthal, S. M. Faber, R. Flores and J. R. Primack, *Astrophys. J.* **301** (1986) 27.
- [80] R. Flores, J. R. Primack, G. R. Blumenthal and S. M. Faber, *Astrophys. J.* **412** (1993) 443.
- [81] H. J. Mo, S. Mao and S. D. M. White, *Mon. Not. Roy. Astron. Soc.* **295** (1998) 319 [arXiv:astro-ph/9707093].
- [82] O. Y. Gnedin, A. V. Kravtsov, A. A. Klypin and D. Nagai, arXiv:astro-ph/0406247.
- [83] W. Dehnen and J. Binney, *Mon. Not. Roy. Astro. Soc.* **294** (1998) 429 [arXiv:astro-ph/9612059].
- [84] A. Klypin, H. Zhao and R. S. Somerville, *Astrophys. J.* **573** (2002) 597 [arXiv:astro-ph/0110390].
- [85] D. Lynden-Bell, *Mon. Not. Roy. Astron. Soc.* **136** (1967) 101.
- [86] S. Tremaine and J. E. Gunn, *Phys. Rev. Lett.* **42** (1979) 407.
- [87] F. H. Shu, *Astrophys. J.* **225** (1978) 83.
- [88] F. H. Shu, *Astrophys. J.* **316** (1987) 502.
- [89] A. Kull, R. A. Treumann and H. Böhringer, *Astrophys. J.* **466** (1996) L1 [arXiv:astro-ph/9606057].
- [90] L. Stodolsky, *Phys. Rev. Lett.* **34** (1975) 110 [Erratum-ibid. **34** (1975) 508].
- [91] N. Cabibbo and L. Maiani, *Phys. Lett. B* **114** (1982) 115.
- [92] P. Langacker, J. P. Leveille and J. Sheiman, *Phys. Rev. D* **27** (1983) 1228.
- [93] I. Ferreras and I. Wasserman, *Phys. Rev. D* **52** (1995) 5459.
- [94] P. F. Smith, in *Trends in Astroparticle Physics*, edited by D. Cline and R. Peccei (World Scientific, Singapore, 1991), p. 311.
- [95] P. F. Smith, *Phil. Trans. Roy. Soc. Lond. A* **361** (2003) 2591.
- [96] C. Hagmann, in *COSMO98: Proceedings of the Conference on Particle Physics and the Early Universe*, edited by D. O. Caldwell (AIP, Woodbury NY, 1999), p.460 [AIP Conf. Proc. **478** (1998) 460; arXiv:astro-ph/9902102].
- [97] C. Hagmann, presented at *American Physical Society (APS) Meeting of the Division of Particles and Fields (DPF 99)*, Los Angeles, USA, 1999, arXiv:astro-ph/9905258.
- [98] J. N. Bahcall, M. H. Pinsonneault and S. Basu, *Astrophys. J.* **555** (2001) 990 [arXiv:astro-ph/0010346].
- [99] M. Honda, T. Kajita, K. Kasahara and S. Midorikawa, *Phys. Rev. D* **70** (2004) 043008 [arXiv:astro-ph/0404457].
- [100] Large Hadron Collider, <http://cern.ch/lhc-new-homepage>
- [101] Very Large Hadron Collider, <http://vlhc.org>
- [102] D. Z. Freedman, *Phys. Rev. D* **9** (1974) 1389.
- [103] B. Müller, in *10th Workshop on Particles and Nuclei: Neutrino Physics*, Heidelberg, Germany, 1987, pp. 269-278.
- [104] A. C. Melissinos, in *Probing Luminous and Dark Matter*, Rochester, USA, 1999, pp. 262-285.
- [105] T. J. Weiler, in *Neutrino Telescopes*, Venice, Italy, 2001, vol. 2, pp. 613-636.
- [106] L. E. Ibáñez, C. Muñoz and S. Rigolin, *Nucl. Phys. B* **553** (1999) 43 [arXiv:hep-ph/9812397].
- [107] M. Gell-Mann, P. Ramond and R. Slansky, in *Supergravity*, edited by D. Z. Freedman *et al.* (North Holland, 1979).
- [108] T. Yanagida, in *Proceedings of Workshop on the Unified Theory and the Baryon Number in the Universe*, KEK, Japan, 1979.
- [109] E. Zavattini, unpublished.
- [110] J. Bernstein, M. Ruderman and G. Feinberg, *Phys. Rev.* **132** (1963) 1227.
- [111] B. P. Konstantinov and G. E. Kocharov, *J. Exp. Theor. Phys.* **19** (1964) 992.
- [112] R. Cowsik, Y. Pal and S. N. Tandon, *Phys. Lett.* **13** (1964) 265.

- [113] T. Hara and H. Sato, *Prog. Theor. Phys.* **64** (1980) 1089.
- [114] T. Hara and H. Sato, *Prog. Theor. Phys.* **65** (1981) 477.
- [115] P. Gondolo, G. Gelmini and S. Sarkar, *Nucl. Phys. B* **392** (1993) 111 [arXiv:hep-ph/9209236].
- [116] E. Roulet, *Phys. Rev. D* **47** (1993) 5247.
- [117] S. Yoshida, H. Y. Dai, C. C. Jui and P. Sommers, *Astrophys. J.* **479** (1997) 547 [arXiv:astro-ph/9608186].
- [118] K. Greisen, *Phys. Rev. Lett.* **16** (1966) 748.
- [119] G. T. Zatsepin and V. A. Kuzmin, *JETP Lett.* **4** (1966) 78 [*Pisma Zh. Eksp. Teor. Fiz.* **4** (1966) 114].
- [120] O. E. Kalashev, V. A. Kuzmin, D. V. Semikoz and G. Sigl, *Phys. Rev. D* **65** (2002) 103003 [arXiv:hep-ph/0112351].
- [121] D. S. Gorbunov, P. G. Tinyakov and S. V. Troitsky, *Astropart. Phys.* **18** (2003) 463 [arXiv:astro-ph/0206385].
- [122] D. V. Semikoz and G. Sigl, *JCAP* **0404** (2004) 003 [arXiv:hep-ph/0309328].
- [123] G. Gelmini, G. Varieschi and T. Weiler, arXiv:hep-ph/0404272.
- [124] Pierre Auger Observatory, <http://www.auger.org/>
- [125] IceCube, <http://icecube.wisc.edu/>
- [126] ANtarctic Impulse Transient Array, <http://www.ps.uci.edu/~anita/>
- [127] Extreme Universe Space Observatory, <http://www.euso-mission.org/>
- [128] Orbiting Wide-angle Light-collectors, <http://owl.gsfc.nasa.gov/>
- [129] Saltdome Shower Array, P. Gorham, D. Saltzberg, A. Odian, D. Williams, D. Besson, G. Frichter and S. Tantawi, *Nucl. Instrum. Meth. A* **490** (2002) 476 [arXiv:hep-ex/0108027].
- [130] T. Reiter, unpublished notes.
- [131] L. N. da Costa, W. Freudling, G. Wegner, R. Giovanelli, M. P. Haynes and J. J. Salzer, *Astrophys. J. Lett.* **468** (1996) L5 [arXiv:astro-ph/9606144].
- [132] A. Dekel *et al.*, *Astrophys. J.* **522** (1999) 1 [arXiv:astro-ph/9812197].
- [133] Akeno Giant Air Shower Array, <http://www.akeno.icrr.u-tokyo.ac.jp/AGASA/>
- [134] K. Abazajian, E. R. Switzer, S. Dodelson, K. Heitmann and S. Habib, arXiv:astro-ph/0411552.
- [135] G. J. Stephenson, T. Goldman and B. H. J. McKellar, *Int. J. Mod. Phys. A* **13** (1998) 2765 [arXiv:hep-ph/9603392].